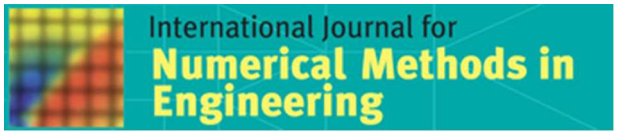

Extended Finite Element Method with Global Enrichment

Journal:	*International Journal for Numerical Methods in Engineering*
Manuscript ID:	Draft
Wiley - Manuscript type:	Research Article
Date Submitted by the Author:	n/a
Complete List of Authors:	Agathos, Konstantinos; Aristotle University Thessaloniki, Civil Engineering Chatzi, Eleni; ETH Zurich, Bordas, Stéphane P.A.; Cardiff University, Institute of Mechanics & Advanced Materials Talaslidis, Demosthenes; Aristotle University Thessaloniki, Dept of Civil Engineering
Keywords:	Finite element methods, Fracture, Solids

Extended Finite Element Method with Global Enrichment

Konstantinos Agathos [a], Eleni Chatzi [b],

Stéphane P. A. Bordas [c,d] and Demosthenes Talaslidis [a]

[a] *Institute of Structural Analysis and Dynamics of Structures, Department of Civil Engineering, Aristotle University Thessaloniki, Panepistimioupolis Mail Stop 502, 54124 Thessaloniki, Greece*

[b] *Institute of Structural Engineering, ETH Zürich, Stefano-Franscini-Platz 5, CH-8093 Zürich, Switzerland*

[c] *Research Unit in Engineering Science, Luxembourg University, 6 rue Richard Coudenhove-Kalergi, L-1359 Luxembourg, Luxembourg*

[d] *Institute of Theoretical, Applied and Computational Mechanics, Cardiff University, Cardiff CF24 3AA, U.K.*

Abstract

A variation of the extended finite element method for 3D fracture mechanics is proposed. It utilizes global enrichment and point-wise as well as integral matching of displacements of the standard and enriched elements in order to achieve higher accuracy, optimal convergence rates and improved conditioning for two and three

dimensional crack problems. A bespoke benchmark problem is introduced to determine the method's accuracy in the general 3D case where it is demonstrated that the proposed approach improves the accuracy and reduces the number of iterations required for the iterative solution of the resulting system of equations by 40% for moderately refined meshes and topological enrichment. Moreover, when a fixed enrichment volume is used, the number of iterations required grows at a rate which is reduced by a factor of 2 compared to standard XFEM, diminishing the number of iterations by almost one order of magnitude.

Key words: XFEM, geometrical enrichment , point-wise matching, dof gathering, global enrichment, conditioning

1 Introduction

It is well known that the simulation of three-dimensional (3D) crack propagation problems using the finite element method (FEM) [1] can be problematic. The difficulties emanate from the fact that the finite element (FE) mesh has to conform to the crack surfaces as well as the boundaries of the analyzed domain. One additional requirement, which further complicates the situation, is that the mesh has to be refined in the vicinity of the crack front in order to

* Corresponding author: stephane.bordas@alum.northwestern.edu (Stéphane P. A. Bordas)

adequately represent the singularity that occurs in the stress fields. Moreover, for every crack propagation step, local remeshing is necessary which makes the whole procedure computationally infeasible.

An alternative to the above procedure, which has produced accurate results, is the boundary element method (BEM)[2] where only the crack surfaces and domain boundaries have to be meshed. The boundary element method has recently been coupled with isogeometric analysis [3,4].

Meshless methods, and more specifically the element free Galerkin (EFG) method [5], have also been applied to crack propagation problems [6] eliminating the need for remeshing and greatly simplifying the process of local refinement. In those methods the concept of "enrichment" [7] was introduced which consists of augmenting the EFG basis in order to include asymptotic near tip fields or special enrichment functions produced from those near tip fields. Several other variations have also been proposed [8,9,10,11] which extend the applicability of the method.

The concept of enrichment combined with the partition of unity property [12] was also employed in the development of the extended finite element method (XFEM) [13,14] which, while retaining the basic properties of the finite element method, does not require any remeshing in order to handle crack propagation problems. Additionally, since asymptotic tip enrichment functions are used, the need for local mesh refinement is minimized. The method

was successfully extended to 3D problems [15,16,17] and industrial problems [18,19,20,21,22].

Since the introduction of the method, numerous attempts have been made towards the improvement of some of the initial method's weaknesses. One of these weaknesses is the lack of optimal convergence which was remedied by enriching elements in a fixed area around the crack tip [23,24,25]. The addition of enriched elements however, leads to poor conditioning of the resulting system matrices which can be solved either by the use of special preconditioners [24,26] or by using the so called degree of freedom (dof) gathering [23] technique. Other drawbacks of the method include blending problems between the enriched and the standard part of the approximation for which several solutions have been given [27,28,29,30,31,32] and problems in numerical integration which can be dealt with by using techniques such as element partitioning and special mappings [23,24,33,34,31,35,36,32,37,38]. Some variations of the method have also been proposed which consist in adding higher order terms of the near tip asymptotic fields in order to directly obtain stress intensity factors [39,40,41]. Finally, significant effort has been devoted in the development of special error estimators and methods for derivative recovery specifically designed for XFEM [42,43,44,45,46].

A variation of the method which successfully handles several of the problems discussed above, is the one proposed by Laborde et al. [23]. The present work is aimed towards extending the concepts developed in the work of Laborde et

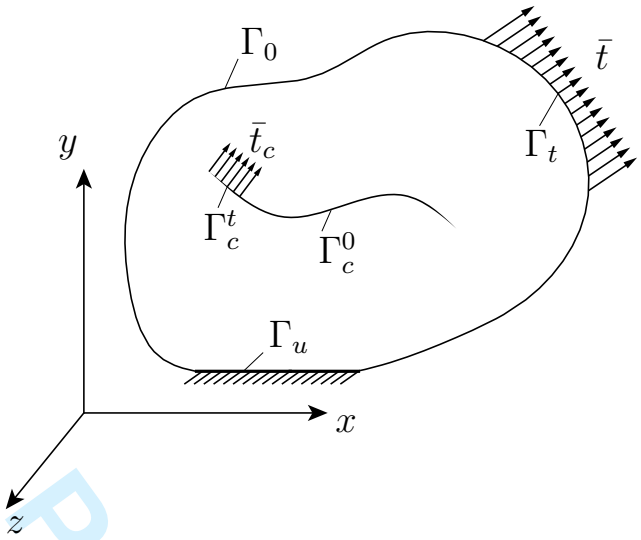

Fig. 1. Cracked Body and boundary conditions.

al. [23] and other similar works [25,47] to three dimensional crack propagation problems, a goal which is not straight forward. The resulting method's accuracy and convergence properties are tested both for the 2D and the 3D case, for the latter a novel benchmark problem is proposed.

2 Problem Statement

The governing equations of the elastostatics problem for a cracked domain will be presented in this section, as well as the weak form of the equilibrium equations.

2.1 Governing equations

Consider the problem of a cracked domain Ω bounded by the boundary Γ consisting of the parts Γ_0, Γ_u, Γ_t and Γ_c where $\Gamma = \Gamma_0 \cup \Gamma_u \cup \Gamma_t \cup \Gamma_c$ and $\Gamma_c = \Gamma_c^t \cup \Gamma_c^0$. The equilibrium equations and boundary conditions are:

$$\begin{aligned}
\boldsymbol{\nabla} \cdot \boldsymbol{\sigma} + \boldsymbol{b} = \mathbf{0} \quad & \text{in} \quad \Omega && \text{(1a)}\\
\boldsymbol{u} = \bar{\boldsymbol{u}} \quad & \text{on} \quad \Gamma_u && \text{(1b)}\\
\boldsymbol{\sigma} \cdot \mathbf{n} = \bar{\boldsymbol{t}} \quad & \text{on} \quad \Gamma_t && \text{(1c)}\\
\boldsymbol{\sigma} \cdot \mathbf{n} = \mathbf{0} \quad & \text{on} \quad \Gamma_c^0 && \text{(1d)}\\
\boldsymbol{\sigma} \cdot \mathbf{n} = \bar{\boldsymbol{t}}_c \quad & \text{on} \quad \Gamma_c^t && \text{(1e)}
\end{aligned}$$

where $\boldsymbol{\sigma}$ is the Cauchy stress tensor, $\mathbf{n}$ is the unit outward normal, $\boldsymbol{b}$ is the body force per unit volume, $\boldsymbol{u}$ is the displacement field and $\boldsymbol{\nabla}$ is the gradient operator. The kinematic equations for small deformations define the strain field $\boldsymbol{\epsilon}$ as the symmetric gradient of the displacement field $\boldsymbol{u}$:

$$\boldsymbol{\epsilon} = \boldsymbol{\nabla}_s \boldsymbol{u} \tag{2}$$

Finally, the constitutive equations are given by Hooke's law:

$$\boldsymbol{\sigma} = \boldsymbol{D} : \boldsymbol{\epsilon} \tag{3}$$

where $\boldsymbol{D}$ is the elasticity tensor.

2.2 Weak Form

For the derivation of the classical finite element formulation, the weak form of the equilibrium equations can be stated as:

Find $\boldsymbol{u} \in \mathcal{U}$ such that $\forall \boldsymbol{v} \in \mathcal{V}^0$

$$\int_\Omega \boldsymbol{\sigma}(\boldsymbol{u}) : \boldsymbol{\epsilon}(\boldsymbol{v})\, d\Omega = \int_\Omega \boldsymbol{b} \cdot \boldsymbol{v}\, d\Omega + \int_{\Gamma_t} \bar{\boldsymbol{t}} \cdot \boldsymbol{v}\, d\Gamma + \int_{\Gamma_c^t} \bar{\boldsymbol{t}}_c \cdot \boldsymbol{v}\, d\Gamma_c^t \tag{4}$$

where :

$$\mathcal{U} = \left\{ \boldsymbol{u} | \boldsymbol{u} \in H^1, \boldsymbol{u} = \bar{\boldsymbol{u}} \text{ on } \Gamma_u \text{ and } \boldsymbol{u} \text{ discontinuous on } \Gamma_c \right\} \tag{5}$$

and

$$\mathcal{V}^0 = \left\{ \boldsymbol{v} | \boldsymbol{v} \in H^1, \boldsymbol{v} = 0 \text{ on } \Gamma_u \text{ and } \boldsymbol{v} \text{ discontinuous on } \Gamma_c \right\} \tag{6}$$

Using the constitutive equations the weak form is obtained as:

Find $\boldsymbol{u} \in \mathcal{U}$ such that $\forall \boldsymbol{v} \in \mathcal{V}^0$

$$\int_\Omega \boldsymbol{\epsilon}(\boldsymbol{u}) : \boldsymbol{D} : \boldsymbol{\epsilon}(\boldsymbol{v})\, d\Omega = \int_\Omega \boldsymbol{b} \cdot \boldsymbol{v}\, d\Omega + \int_{\Gamma_t} \bar{\boldsymbol{t}} \cdot \boldsymbol{v}\, d\Gamma + \int_{\Gamma_c^t} \bar{\boldsymbol{t}}_c \cdot \boldsymbol{v}\, d\Gamma_c^t \tag{7}$$

3 Global enrichment XFEM

The method presented in this work can be viewed as an extension of the method proposed by Laborde et al. [23] since some basic aspects such as point-wise matching, degree of freedom (dof) gathering and geometrical enrichment (enrichment in a fixed area around the crack tip/front) are common in both methods. However, since this work is aimed towards a broader spectrum of applications, including three dimensional problems, several modifications/extensions are made to the original method. We first recall the general ideas of the work of Laborde et al. [23] before introducing the aforementioned modifications. It should be noted however, that while in the method of Laborde et al. [23] higher order elements are considered, in the present work only linear (P1) elements are used.

3.1 The method of Laborde

In the work of Laborde et. al it was observed that by enriching elements in a fixed area around the crack tip, an optimal convergence rate could be achieved. The above enrichment strategy, in the work of Béchet et al. [24], was referred to as "geometrical enrichment" as opposed to "topological enrichment" where only a layer of elements around the crack tip is enriched.

The addition of layers of tip enriched elements however, would lead to a drastic deterioration in the conditioning of the resulting system matrices. As a remedy, dof gathering was proposed which consists in using a global function to weigh the enrichment functions rather than the shape functions of tip enriched elements. This function is equal to 1 for all nodes lying inside the enrichment area, assumes a value of 0 for all nodes outside the enrichment area and varies linearly in-between. While this technique leads to a decreased number of additional dofs and improved conditioning, it also leads to sub-optimal convergence rates.

The lack of optimal convergence was attributed to the problems occurring in the transition layer between enriched and regular elements. These problems were resolved by eliminating the transition layer of elements and matching displacements between enriched and regular elements. The method used to match displacements was point-wise matching.

The above concepts in addition to an improved numerical integration scheme lead to a method of increased accuracy which provided optimal convergence rates and improved conditioning. The equations related to the above ideas, as well as the modifications and extensions made, will be presented in detail in the following subsections.

3.2 Crack representation

The proposed method is independent of the crack representation used. Consequently, any of the available possibilities can be used such as level sets [16,17,48], vector level sets [49] or a hybrid explicit implicit representation [50].

For the simple examples treated in this work, a level set representation [16,17,48] was used and enrichment functions were evaluated using finite element approximation of the level set functions as is commonly done in XFEM.

In the following subsections the level set functions will be denoted as ϕ and ψ where, given an arbitrary point $\mathbf{x}$ in the domain:

- $\phi(\mathbf{x})$ is the signed distance from the crack surface
- $\psi(\mathbf{x})$ is a signed distance function such that $\nabla\phi \cdot \nabla\psi = 0$ and $\phi(\mathbf{x}) = 0$ and $\psi(\mathbf{x}) = 0$ defines the crack front.

The polar coordinates used for the definition of the enrichment functions are defined as [16,17,48]:

$$r = \sqrt{\phi^2 + \psi^2}, \qquad \theta = \arctan\left(\frac{\phi}{\psi}\right) \tag{8}$$

3.3 Tip enrichment

The most important extension made to the method of Laborde et al. [23], which enables the application of the idea to 3D problems, is related to the tip enrichment scheme used and more specifically to dof gathering. In the aforementioned method, tip enrichment functions were weighted by a global function assuming a value of 1 for all tip enriched elements in order to decrease the number of additional unknowns and improve the conditioning of the resulting matrices. The above approach does not allow any spatial variation of the tip enrichment functions. Nevertheless, in 3D problems, solution parameters such as stress intensity factors (SIFs) vary along the crack front making the direct extension of the method, as presented in [23], to 3D impossible.

In the present work, a novel approach is introduced for weighting tip enrichment functions consisting of some global shape functions which allow spatial variability of the enrichment functions along the crack front but not in any other direction, thus preserving the advantages yielded by dof gathering and enabling the use of geometrical enrichment in 3D problems. The enriched part of the displacement approximation for tip enriched elements, evaluated at $\mathbf{x} \in \Omega$, can then be written as:

$$\mathbf{u_t}\left(\mathbf{x}\right) = \sum_k N_K^g\left(\mathbf{x}\right) \sum_j F_j\left(\mathbf{x}\right) \mathbf{c}_{Kj} \tag{9}$$

where N_K^g are the global shape functions which refer to a superimposed mesh of special elements and will be presented in detail in Section 3.8, index K refefers to nodes of the superimposed mesh, F_j are tip enrichment functions and $\mathbf{c}_{kj}$ are the corresponding tip dofs. Tip enrichment functions are defined as in standard XFEM:

$$F_j(\mathbf{x}) \equiv F_j(r,\theta) = \left[\sqrt{r}\sin\frac{\theta}{2}, \sqrt{r}\cos\frac{\theta}{2}, \sqrt{r}\sin\frac{\theta}{2}\sin\theta, \sqrt{r}\cos\frac{\theta}{2}\sin\theta\right] \quad (10)$$

The precise definition of parameters r and θ was given in Subsection 3.2. For two dimensional problems, the above approach coincides with dof gathering.

In order to apply geometrical enrichment the radius of enrichment r_e has to be defined. Subsequently, nodal values r_i of variable r are computed. If the condition $r_i < r_e$ is true for every node of a given element, then the element is tip enriched (Figure 1).

3.4 Jump enrichment

Throughout this work shifted jump enrichment functions are used [51,19]. Moreover the jump enrichment functions are defined as:

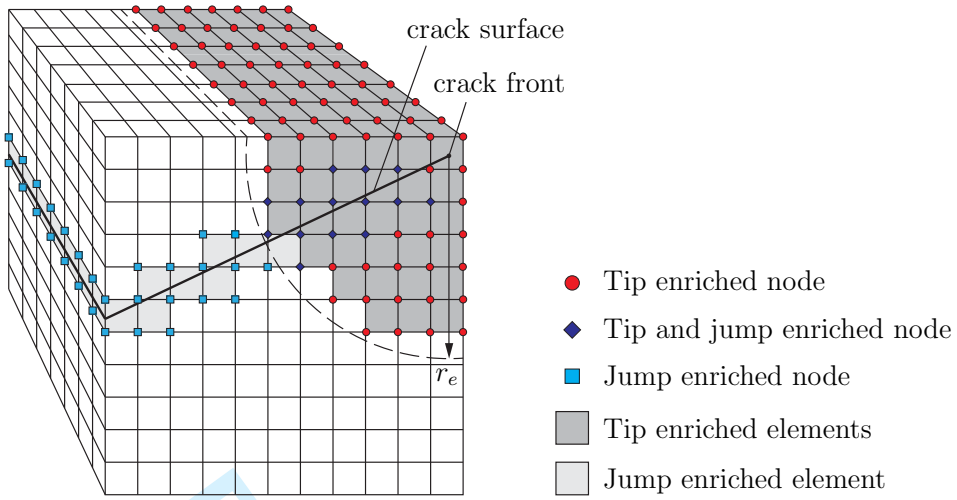

Fig. 2. Enrichment strategies used for tip and jump enrichment.

$$H(\phi) = \begin{cases} 1 & \text{for } \phi > 0 \\ -1 & \text{for } \phi < 0 \end{cases} \tag{11}$$

The definition of ϕ was given in Subsection 3.2.

The nodal set of jump enriched nodes is defined in a slightly different way than in standard XFEM. In order to justify the proposed approach some important facts have to be considered. More specifically, the tip enrichment functions used (Equation 10) are derived from the first term of the Williams expansion and represent displacements in the vicinity of the crack tip. However, in the general case, displacements around the crack tip consist of higher order terms as well. This is especially true for the case where geometrical enrichment with relatively large enrichment radii is used. Such higher order terms are also essential when computing T-stresses. In standard XFEM those higher order terms can be represented by the FE part of the approximation, in addition since the

tip enrichment functions are weighted by the FE shape functions, some additional flexibility is added, allowing the method to approximate higher order terms by spatially adjusting the coefficients of the enrichment functions. In the proposed method, higher order terms can only be approximated by the FE part of the approximation, since no spatial variation of the tip enrichment function coefficients is allowed in the plane normal to the crack front due to the fact that all the coefficients (dofs) premultiplying the enrichment functions vary only in the direction of the crack front. As a result, in elements which contain the crack surfaces, displacement jumps caused by higher order terms can not be represented. In other words, in elements that are tip enriched and contain the crack surfaces, crack opening displacements can only assume the form imposed by the tip enrichment terms.

The above situation has a negative impact on accuracy, and in order to remedy this issue we introduce a special enrichment strategy which consists in using both tip and jump enrichment functions for elements that contain the crack and lie inside the area of enrichment (Figure 1). By employing this strategy, crack opening displacements caused by higher order terms can be represented in tip elements through jump enrichment functions whose weights are allowed to vary spatially.

The aforementioned difficulties and associated improvements obtained by the proposed solution will be demonstrated through a numerical example in Section 4.

3.5 Point-wise matching

The basic idea behind point-wise matching, which lies in directly matching displacements between tip and jump enriched or tip enriched and regular elements in order to avoid errors in blending elements, is retained in this work. The implementation however is adapted to the specific demands of the proposed approach.

3.5.1 Tip and Regular Elements

Firstly, displacement approximations of regular and tip enriched elements are considered:

$$\mathbf{u_r}(\mathbf{x}) = \sum_I N_I(\mathbf{x})\,\mathbf{u}_I + \sum_J N_J(\mathbf{x})\,\mathbf{a}_J \tag{12a}$$

$$\mathbf{u_t}(\mathbf{x}) = \sum_I N_I(\mathbf{x})\,\mathbf{u}_I + \sum_K N_K^g(\mathbf{x}) \sum_j F_j(\mathbf{x})\,\mathbf{c}_{Kj} \tag{12b}$$

where N_I are FE shape functions, $\mathbf{u}_I$ are standard FE dofs (nodal displacements) and $\mathbf{a}_J$ are additional parameters to be determined. Indices I and J vary over the set of nodes that are common between tip enriched and regular elements, while index K refers to the nodes of the superimposed mesh.

Subsequently, displacements are matched by imposing the condition [1]:

[1] Note that this procedure also removes completely blending errors [27,28,29,30,31,32].

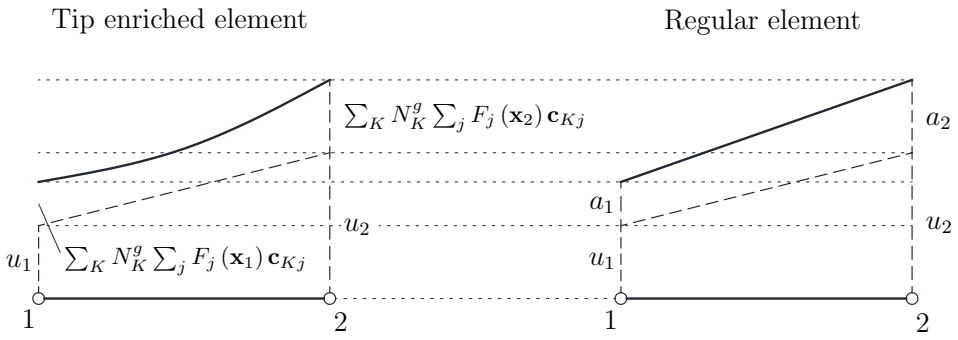

Fig. 3. Displacements along the edges of tip enriched and regular elements.

$$\mathbf{u_r}(\mathbf{x}) = \mathbf{u_t}(\mathbf{x}) \tag{13}$$

at nodal points that are common between tip enriched and regular elements. From the above constraint, the parameters $\mathbf{a}_i$ are determined:

$$\mathbf{a}_I = \sum_k N_K^g(\mathbf{X}_I) \sum_j F_j(\mathbf{X}_I)\mathbf{c}_{Kj} \tag{14}$$

where $F_j(\mathbf{X}_I)$ are the tip enrichment functions evaluated at nodal point $\mathbf{X}_I$.

The above procedure is illustrated in Figure 2 where the displacements of a common edge between a tip enriched and a regular element are depicted.

From the above, it should be clear that parameters $\mathbf{a}_I$ do not correspond to any additional dofs since they are expressed in terms of the tip dofs $\mathbf{c}_{Kj}$. Thus Equation 14 can be reformulated as:

$$\mathbf{a}_I = \sum_K \sum_j T_{IKj}^{t-r}\mathbf{c}_{Kj} \tag{15}$$

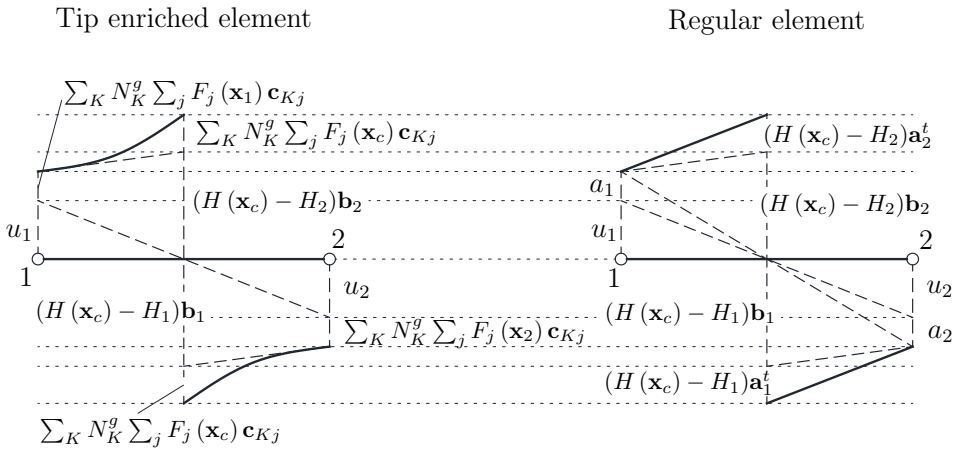

Fig. 4. Displacements along the edges of tip and jump enriched elements.

where T_{IKj}^{t-r} are the components of a matrix correlating the two sets of parameters.

3.5.2 Tip and Jump Elements

Throughout this work shifted jump enrichment functions are used which assume a value of zero at nodal points. As a result, point-wise patching has to be adapted accordingly. More precisely, displacements for the jump and tip enriched elements are (Figure 3):

$$\mathbf{u_j}(\mathbf{x}) = \sum_I N_I(\mathbf{x})\,\mathbf{u}_I + \sum_J N_J(\mathbf{x})\,\mathbf{a}_J + \sum_K N_K(\mathbf{x})\,(H(\mathbf{x}) - H_K)\mathbf{b}_K + + \sum_L N_L(\mathbf{x})\,(H(\mathbf{x}) - H_L)\mathbf{b}_L^t\,, \tag{16a}$$

$$\mathbf{u_t}(\mathbf{x}) = \sum_I N_I(\mathbf{x})\,\mathbf{u}_I + \sum_J N_J(\mathbf{x})\,(H(\mathbf{x}) - H_J)\mathbf{b}_J + + \sum_K N_K^g(\mathbf{x}) \sum_j F_j(\mathbf{x})\,\mathbf{c}_{Kj} \tag{16b}$$

where $\mathbf{b}_K$ are jump dofs, $\mathbf{b}_L^t$ are additional parameters to be determined, H

is the Heaviside function, H_K is the jump enrichment function evaluated at node K.

As already mentioned, tip enriched elements that contain the crack are also jump enriched. Moreover, parameters $\mathbf{b}_I^t$ hold a similar role to parameters $\mathbf{a}_I$ and have to be determined. One possibility would be to treat those parameters as additional dofs and let their values be determined as part of the solution. However, our experience shows that this leads to a reduced accuracy. An alternative procedure is introduced where those parameters are obtained in terms of the tip dofs by imposing additional constraints at points located at elements edges or faces (for 3D elements).

The point-wise matching condition assumes the form:

$$\mathbf{u_j}\left(\mathbf{x}\right) = \mathbf{u_t}\left(\mathbf{x}\right) \tag{17}$$

at selected points in the domain. By evaluating the above condition at nodal points parameters $\mathbf{a}_I$ are obtained as in Equation 14. By evaluating the condition at the additional points, parameters $\mathbf{b}_I^t$ are obtained:

$$\left(H(\mathbf{X}_l) - H_I\right)\mathbf{b}_I^t = \sum_k N_K^g(\mathbf{X}_l)\sum_j F_j(\mathbf{X}_l)\mathbf{c}_{Kj} - \sum_I N_I(\mathbf{X}_l)\mathbf{a}_I \tag{18}$$

where $F_j(\mathbf{X}_l)$ are the tip enrichment functions evaluated at the additional points $\mathbf{X}_l$ and $H(\mathbf{X}_l)$ are the jump enrichment functions evaluated at the

additional points $\mathbf{X}_l$.

It should be noted that Equation 18 represents a linear system of equations. Nevertheless, due to the properties of shifted jump enrichment functions, the equations are decoupled in most cases.

In a similar fashion to Equation 14 and by taking into account Equation 15, Equation 18 can be reformulated as:

$$\mathbf{b}_I^t = \sum_k \sum_j T_{IKj}^{t-j} \mathbf{c}_{Kj} \tag{19}$$

where T_{IKj}^{t-r} are the components of a matrix which comes from the solution of Equation 18.

An important step in the whole procedure is the selection of points where the additional condition is applied. The basic restriction that applies in the selection of those points is imposed by the fact that shifted enrichment functions vanish on one side of the crack and as a result the corresponding points have to be selected on the opposite side in order to prevent the coefficient matrix of Equation 18 from being singular.

In this work, the points for the additional constraint are chosen to be the points where the two surfaces of the crack intersect element edges or faces. In order to locate those points, for each edge where the additional condition has to be applied, the point where the first level set assumes a value of zero

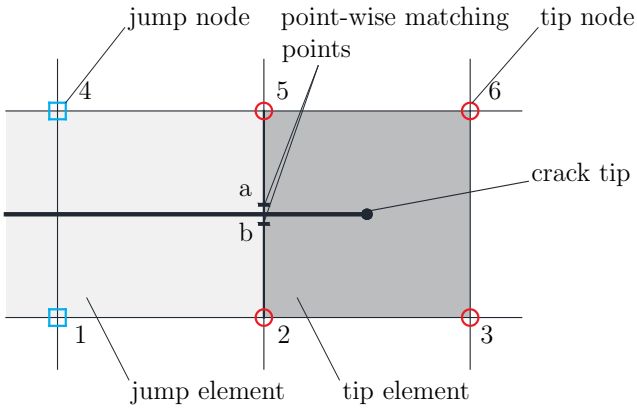

Fig. 5. Selection of points for the imposition of the additional point-wise matching condition in quadrilateral elements. The additional condition is imposed at points a and b.

is initially located. Subsequently, this point is moved by a small increment towards either side of the crack. It should be noted that the size of this increment has negligible effect in the accuracy and/or behavior of the method. In our numerical experiments a value of 10^{-8} in the isoparametric coordinate system was used.

This selection procedure is illustrated in Figure 4 for the 2D case, where point-wise matching is taking place in the edge defined by nodes 2 and 5. The points selected are points **a** and **b** where parameters $\mathbf{b}_2^t$ and $\mathbf{b}_5^t$ corresponding to nodes 2 and 5 are defined respectively.

For the 3D case the selection of points is somehow more involved due to the complex geometry. For linear hexahedral elements, which are used in this work, point-wise matching can take place at an edge, a face, several faces or edges and combinations of faces and edges as illustrated in Figure 5.

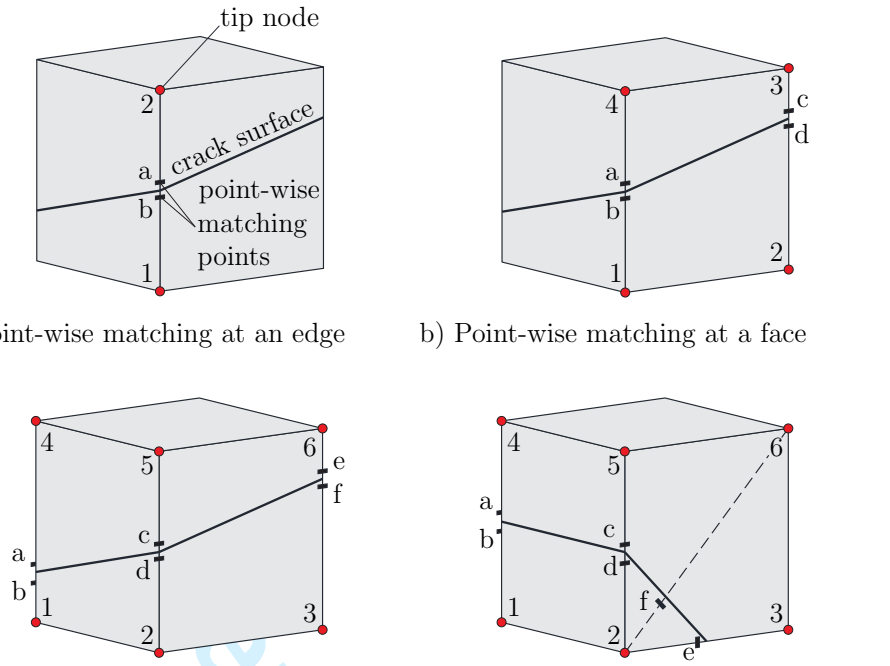

a) Point-wise matching at an edge b) Point-wise matching at a face

c) Point-wise matching at several faces d) Point-wise matching at several faces

Fig. 6. Selection of points for the imposition of the additional point-wise matching condition in a hexahedral element for four different cases. The additional condition is imposed at points a-f.

The selection of points, which is also demonstrated in Figure 5 is performed in a similar way as for the 2D case. An additional requirement is that in the case where point-wise matching takes place in several faces (Figure 5 (c) and (d)), the selected points must coincide at edges that are common in those faces.

A case of special interest is the one of Figure 5 (d). In particular, at point f which corresponds to node 6, the enrichment functions of nodes 3 and 5 do not vanish and as a result the system of Equation 18 is no longer decoupled for face 2-3-6-5.

The situation depicted in Figure 6 is also particularly significant. In this case,

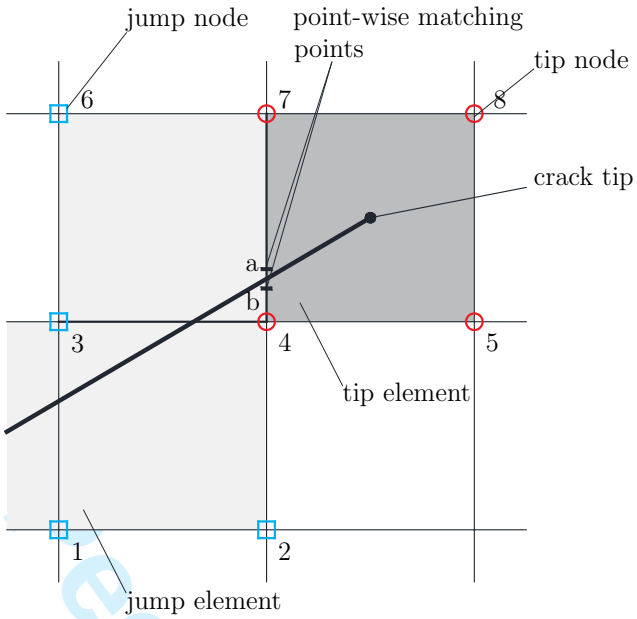

Fig. 7. Special case for the selection of points for the additional point-wise matching condition.

point-wise matching would take place at the edges defined by nodes 3, 4 and 4, 7. However, the edge defined by nodes 3 and 4 does not belong to a tip enriched element and as a result evaluating the tip enrichment functions for a point on that edge would lead to errors. In order to avoid these errors, the values of the parameters $\mathbf{b}_4^t$ obtained from edge 4-7 should be also used for edge 3-4. Of course, similar situations occur also in the 3D case.

In order to implement the procedure described above, all elements where point-wise matching occurs, should be identified and looped over prior to the assembly of the stiffness matrix and wherever possible the values of the parameters $\mathbf{b}_i^t$ should be computed and stored. This way, the parameters $\mathbf{b}_i^t$ can be computed for every node using the correct element edges or faces. Moreover, the whole procedure is computationally inexpensive.

3.6 Integral matching

The proposed method is intended to be used both with geometrical and topological enrichment. In the latter case, for the P1 (linear) elements used in the present work, a loss of accuracy is observed, which is more pronounced for mode I loading. This can attributed to the geometry of the deformation and more specifically to the displacement jump between regular and tip enriched elements. This displacement jump also occurs for mode II crack loading, however in that case it can be considered to vanish in a weak (integral) sense, as illustrated in Figure 8 , and as a result the loss of accuracy is smaller.

One possible solution to the problem is the addition of one layer of enriched elements around the crack tip/front. An alternative solution is proposed here which consists of the addition of hierarchical blending functions. Those functions are added to elements where point-wise matching occurs and serve the purpose of eliminating the displacement jump in a weak sense.

For linear quadrilateral elements those functions assume the form:

$$N^h\left(\xi_1,\xi_2\right)=\frac{\left(1-\left|\xi_1\right|\right)\left(1+\xi_2\right)}{2} \tag{20}$$

where ξ_1 and ξ_2 are the element's isoparametric coordinates. Variables ξ_1 and ξ_2 in the the above equation as well as their signs change depending on the side on which the blending functions are added. For 3D brick elements those

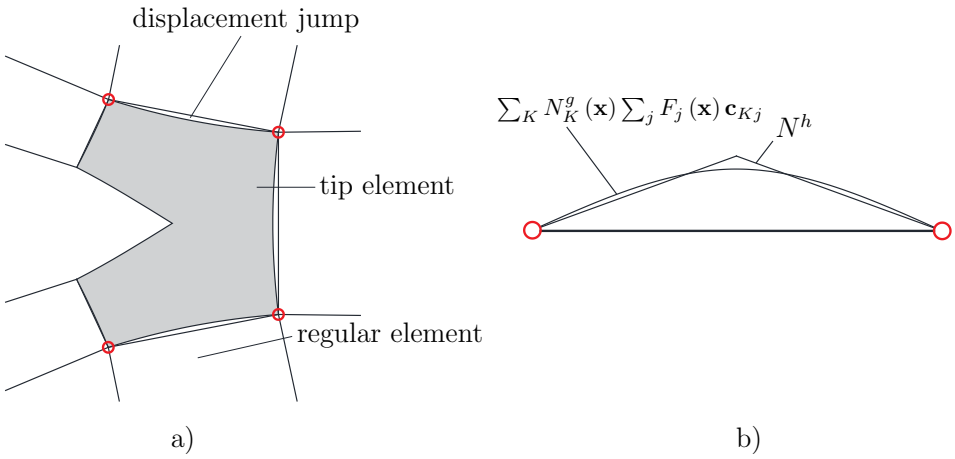

Fig. 8. a) Displacement jump along element edges. b) Hierarchical blending functions.

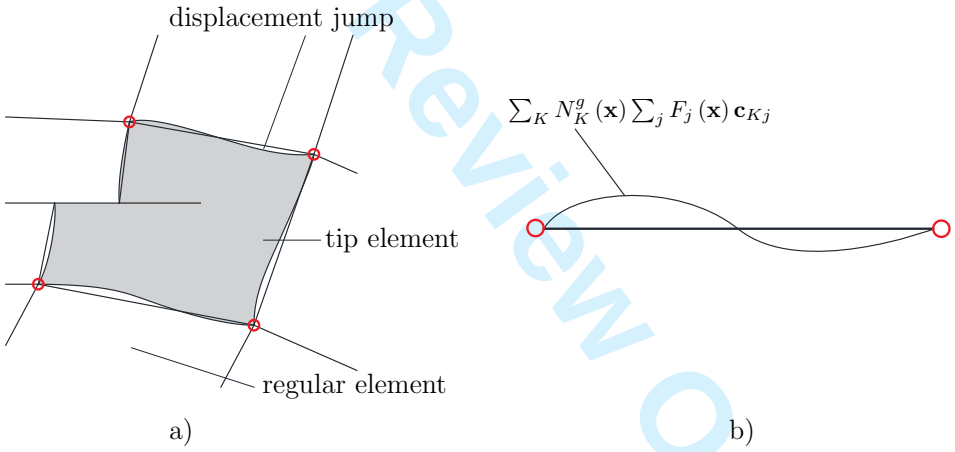

Fig. 9. a) Displacement jump along element edges. b) Displacements along an element edge. It can be seen that gaps as well as overlaps occur which result in the discontinuity almost vanishing in a weak sense.

functions assume a similar form.

Adding to the approximation the blending functions, displacements along the

edges of regular and jump enriched elements take the form:

$$\mathbf{u_r}\left(\xi_1,\xi_2\right)=\sum_I N_I\left(\xi_1,\xi_2\right)\mathbf{u}_I+\sum_J N_J\left(\xi_1,\xi_2\right)\mathbf{a}_J+N^h\left(\xi_1,\xi_2\right)\mathbf{a}^h \tag{21a}$$

$$\mathbf{u_t}\left(\xi_1,\xi_2\right)=\sum_I N_I\left(\xi_1,\xi_2\right)\mathbf{u}_I+\sum_K N_K^g\left(\mathbf{x}\right)\sum_j F_j\left(\mathbf{x}\right)\mathbf{c}_{Kj} \tag{21b}$$

where $\mathbf{a}^h$ are the coefficients of the blending functions.

Those coefficients could be obtained by imposing a point-wise matching condition in the midpoints of element edges which is similar to the approach used in previous subsections. It was observed however that an increased accuracy can be obtained in the general 3D case by applying an integral matching condition of the form:

$$\int_S\left(\mathbf{u_r}-\mathbf{u_t}\right)dS=0 \tag{22}$$

where S is the element edge length.

This approach shares some similarities with the work of Chanine et al. [47]. Nonetheless, in the present case integral matching is only used for the additional blending functions and nodal displacements are matched using point-wise matching.

In a similar fashion as in the previous subsections, coefficients $\mathbf{a}^h$ can be obtained as functions of the tip dofs:

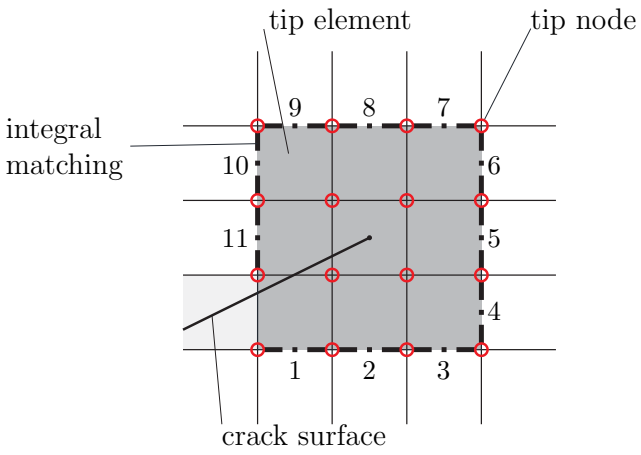

Fig. 10. Imposition of integral matching condition. Integral matching takes place along edges $1-11$. The coefficients used for integral matching would be $\mathbf{a}_1^h - \mathbf{a}_{11}^h$, where the indices refer to edges $1-11$.

$$\mathbf{a}_i^h = \sum_K \sum_j T_{iKj}^h \mathbf{c}_{Kj} \tag{23}$$

In the above relation, index i refers to edges and not nodes (Figure 9).

In the general 3D case additional functions could be added to match displacements along faces as well. In the present implementation however only matching along edges was implemented.

For cases where the crack tip/front is in the close vicinity of element nodes, the method's accuracy decreases despite the use of those functions. In those cases neighboring elements should be tip enriched as well in order to prevent this loss of accuracy.

3.7 Displacement approximation

Summarizing all the above, the displacement approximation for the whole domain can be formulated as:

$$\mathbf{u}(\mathbf{x}) = \sum_{I\in\mathcal{N}} N_I(\mathbf{x})\,\mathbf{u}_I + \sum_{J\in\mathcal{N}^j} N_J(\mathbf{x})\,(H(\mathbf{x}) - H_J)\mathbf{b}_J + \\ + \sum_{K\in\mathcal{N}^s} N_K^g(\mathbf{x}) \sum_j F_j(\mathbf{x})\,\mathbf{c}_{Kj} + \mathbf{u}^{pm}(\mathbf{x}) + \mathbf{u}^{im}(\mathbf{x}) \tag{24a}$$

$$\mathbf{u}^{pm}(\mathbf{x}) = \sum_{I\in\mathcal{N}^{t1}} N_I(\mathbf{x}) \sum_K \sum_j T_{IKj}^{t-r}\mathbf{c}_{Kj} + \\ + \sum_{J\in\mathcal{N}^{t2}} N_J(\mathbf{x})\,(H(\mathbf{x}) - H_J) \sum_K \sum_j T_{IKj}^{t-j}\mathbf{c}_{Kj} \tag{24b}$$

$$\mathbf{u}^{im}(\mathbf{x}) = \sum_{I\in\mathcal{N}^h} N_I^h(\mathbf{x}) \sum_K \sum_j T_{IKj}^{h}\mathbf{c}_{Kj} \tag{24c}$$

The sets mentioned in the above equation are defined as follows:

$\mathcal{N}$ is the set of all nodes in the FE mesh.

$\mathcal{N}^j$ is the set of jump enriched nodes. This set includes all nodes whose shape function support is divided in two by the crack. This definition does not change when geometrical enrichment is used as discussed in Subsection 3.4.

$\mathcal{N}^s$ is the set of superimposed nodes. This set does not refer to nodes of the FE mesh but to nodes of the superimposed mesh which will be described in the next section.

$\mathcal{N}^{t1}$ is the set of transition nodes between tip and regular and jump elements.

$\mathcal{N}^{t2}$ is the set of transition nodes between tip and jump elements.

$\mathcal{N}^h$ is the set of edges where the blending functions are added.

3.8 Definition of the Front Elements

In this subsection, the definition of the superimposed mesh and the corresponding shape functions N_K^g mentioned in Subsection 3.3 are given.

3.8.1 Approximation along the crack front

The superimposed mesh introduced in this work serves the purpose of providing a basis with which the singular enrichment functions will be weighted. The desired properties for this basis are that it should satisfy the partition of unity property, and additionally that it should allow spatial variation only along the direction of the crack front. Those requirements can be fulfilled by elements that share properties of both one-dimensional and three-dimensional elements. Those elements are one-dimensional in the sense that their shape functions allow variation only along one dimension and are defined by two nodes (more if higher order elements are used), and are three-dimensional in the sense that their shape functions are defined in a three-dimensional domain and as a result additional information other than their nodal coordinates is required for their definition. An alternative way to view those elements, would be as 3D brick elements with their nodes constrained in a way such that variation along only one dimension is allowed.

A concept which is very similar to the superimposed mesh used in this work, is the analytical patch and the corresponding nodes and elements used in the work of Langlois et al.[52]. The method also shares some similarities with the s-finite element method [53], it differs however from both methods since in the present method the superimposed mesh is only used to provide a basis for weighting the singular enrichment functions. For this reason the superimposed elements have no particular physical meaning other than that of providing a means to introduce spatial variation of the enrichment functions.

For the definition of the superimposed mesh, a set of points that lie on the crack front have to be identified. The appropriate thickness of the front elements has to be determined depending on the variability of the SIFs along the front.

As far as the identification of the points on the crack front is concerned, the location of such points is usually required also for the calculation of SIFs. Moreover, the use of a hybrid crack representation [50] would further facilitate the whole procedure since this hybrid approach consists of meshing the crack and as a result the location and connectivity of the points required for meshing the crack front would be already available. Of course, a more dense discretization of the crack front might be necessary, in which case some refinement would be needed.

In the present work, only linear elements were implemented for meshing of the

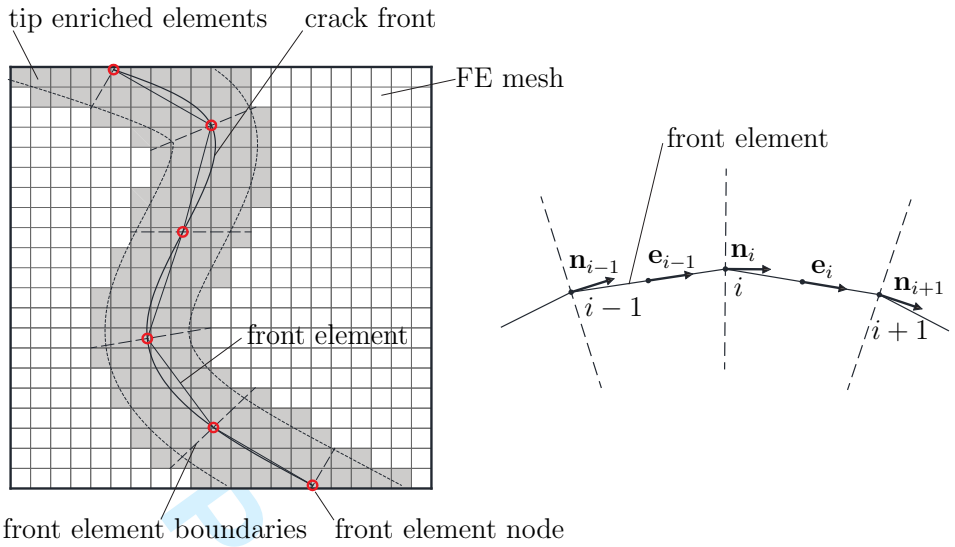

Fig. 11. a)Crack front discretization for open crack fronts. b) Vectors associated with front elements

crack front. Several alternatives are possible for the definition of front element boundaries. In the next subsections two approaches will be presented which are best suited for open and closed crack fronts respectively. Moreover, for both approaches continuous numbering of the front nodes will be assumed.

3.8.1.1 Open crack fronts Elements are defined by two consecutive nodes and element boundaries are defined in the following way (see also Figure 10):

- For every element a unit vector $\mathbf{e_i}$ is defined parallel to the direction of the line connecting the two nodes belonging to the element: $\mathbf{e_i} = \frac{\mathbf{x_{i+1}} - \mathbf{x_i}}{|\mathbf{x_{i+1}} - \mathbf{x_i}|}$.
- For every nodal point i a unit vector $\mathbf{n_i}$ is defined as the mean of the two vectors corresponding to the elements adjacent to the node: $\mathbf{n_i} = \frac{\mathbf{e_i} + \mathbf{e_{i-1}}}{|\mathbf{e_i} + \mathbf{e_{i-1}}|}$.
- Additionally, a plane is defined that passes through the node and is nor-

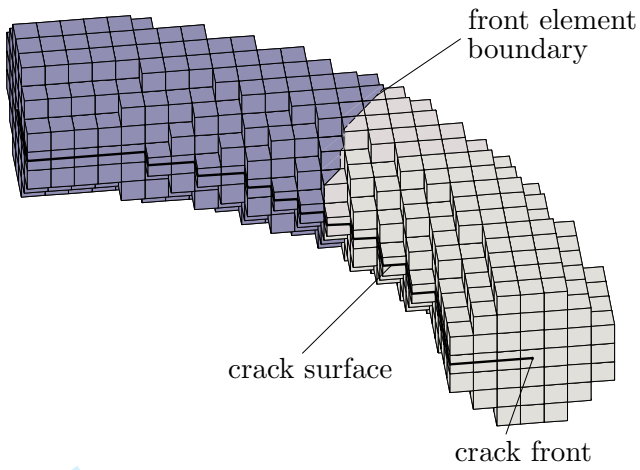

Fig. 12. Volume corresponding to two consecutive front elements. Different element colors correspond to different front elements.

mal to the vector $\mathbf{n_i}$ corresponding to the node: $\mathbf{n_i} \cdot (\mathbf{x_0} - \mathbf{x_i}) = 0$.

- The volume corresponding to the element is defined by the planes corresponding to its nodes and the tip enriched elements around the crack front. The geometry of front elements is illustrated in Figure 10 (a) and in Figure 11 where part of a curved crack front is shown along with the tip enriched element and the corresponding front element volumes.

In order to deal with cases were the crack intersects with free surfaces, the first and/or last node can be moved in the direction of the crack front so that all finite elements within the radius of interest lie inside the first and/or last superimposed element.

3.8.1.2 Closed crack fronts For closed crack fronts the above approach might lead to certain difficulties. More specifically, if the elliptical crack of Figure 12 is considered, the element boundaries defined by the above approach

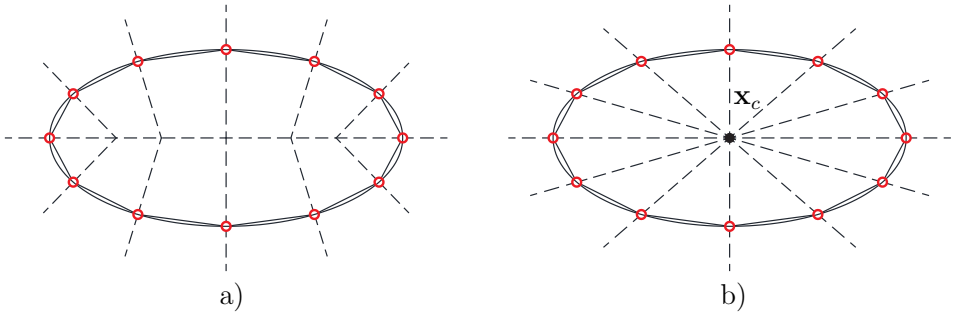

Fig. 13. a) Application of the method used for open crack fronts to closed crack fronts, it can be seen that front elements overlap. b) Method used for closed crack fronts, it can be seen that ovelaps are avoided.

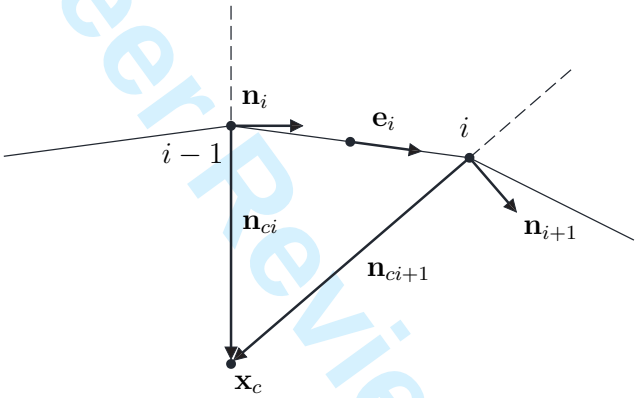

Fig. 14. Front element boundadries for closed crack fronts.

and depicted in Figure 12 (a) overlap which could cause problems in the definition of front element boundaries if the area used for tip enrichment is large enough to include the point where this overlapping occurs. In order to avoid similar situations, a different approach is adopted according to which, element boundaries are defined by using an additional point ($\mathbf{x_c}$) in the interior of the closed curve defined by the crack front as in Figure 12 (b). For plane cracks this point lies on the crack surface.

In more detail (see also Figure 13):

- Vectors $\mathbf{e_i}$ are defined for every element.
- A point $\mathbf{x_c}$ in the interior of the crack front is defined as: $\mathbf{x_c} = \frac{\sum_{i=1}^{n} \mathbf{x_c}}{n}$.
- For every nodal point i, a vector $\mathbf{n_{ci}}$ joining that point to the internal point $\mathbf{x_c}$ is defined: $\mathbf{n_{ci}} = \mathbf{x_c} - \mathbf{x_i}$.
- Vectors $\mathbf{n_{ni}}$ normal to the plane defined by vectors $\mathbf{e_i}$ and $\mathbf{n_{ci}}$ are defined as: $\mathbf{n_{ni}} = \mathbf{e_i} \times \mathbf{n_{ci}}$.
- Vectors $\mathbf{n_i}$ are defined as: $\mathbf{n_i} = \frac{\mathbf{n_{ti}} \times \mathbf{n_{ci}}}{|\mathbf{n_{ti}} \times \mathbf{n_{ci}}|}$.
- Planes normal to the vectors $\mathbf{n_i}$ are defined: $\mathbf{n_i} \cdot (\mathbf{x_0} - \mathbf{x_i}) = 0$.
- Element volumes are defined by the planes corresponding to their nodes as for the open crack front case.

As already mentioned, superimposed elements have no particular physical meaning, nevertheless it is important to define their boundaries so as to be able to relate every enriched element to its corresponding superimposed elements.

The problem described for closed cracks can also occur for open cracks or parts of open cracks where the curvature of the crack front is large or if sharp corners are present. In that case the closed crack front approach should be used. The definition of point $\mathbf{x_c}$ however, will have to be adjusted accordingly.

3.8.2 Front element parameter

In order to facilitate the interaction of the XFEM and crack front meshes, one additional function, similar to the level sets, is defined which varies along the

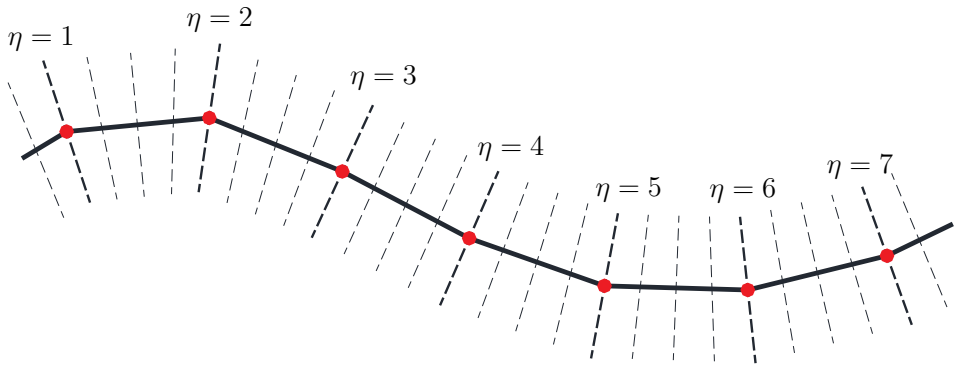

Fig. 15. Iso lines of the front element parameter.

direction of the crack front. This parameter takes integer values on the front nodes and the planes defined by front nodes and varies linearly in-between (Figure 14). Since front nodes are numbered continuously, the values of the parameter at the nodes should coincide with node numbers.

For a point $\mathbf{x_0}$ this parameter is evaluated as follows:

For all front elements the plane equations corresponding to their nodes are evaluated:

$$f_i(\mathbf{x_0}) = \mathbf{n_i} \cdot (\mathbf{x_0} - \mathbf{x_i}) \tag{25a}$$
$$f_{i+1}(\mathbf{x_0}) = \mathbf{n_{i+1}} \cdot (\mathbf{x_0} - \mathbf{x_{i+1}}) \tag{25b}$$

- If $f_i < 0$ or $f_{i+1} > 0$ the point lies outside the element volume and the next element is checked.
- If $f_i = 0$ or $f_{i+1} = 0$ the point lies on the plane corresponding to node i or $i + 1$ respectively and it is assigned a front parameter value $\eta = i$ or $\eta = i + 1$.
- If $f_i > 0$ and $f_{i+1} < 0$ the point lies inside the element.

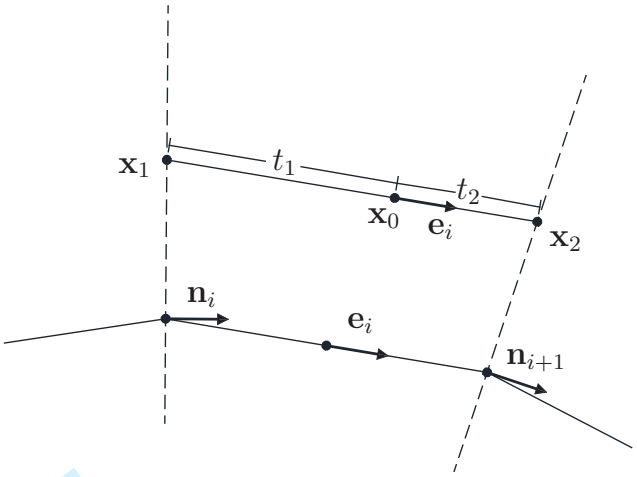

Fig. 16. Front element parameter evaluation.

If the point is found to lie inside a certain element (Figure 15), the integer part of the front parameter is equal to the number of the first element node $\eta_i = i$. In order to evaluate the fractional part of the parameter a line is formed which passes from point $\mathbf{x_0}$ and is parallel to vector $\mathbf{e_i}$. Points on this line have coordinates:

$$\mathbf{x} = \mathbf{x_0} + t\mathbf{e_i} \qquad t \in \mathbb{R} \tag{26}$$

where t is the line parameter.

At the point where the line intersects the planes defined by element nodes, parameter t takes the values:

$$t_1 = \frac{\mathbf{n_i} \cdot (\mathbf{x_0} - \mathbf{x_i})}{\mathbf{n_i} \cdot \mathbf{e_i}} \tag{27a}$$

$$t_2 = \frac{\mathbf{n_{i+1}} \cdot (\mathbf{x_0} - \mathbf{x_{i+1}})}{\mathbf{n_{i+1}} \cdot \mathbf{e_i}} \tag{27b}$$

The coordinates of those points are:

$$\mathbf{x_1} = \mathbf{x_0} + t_1 \mathbf{e_i} \tag{28a}$$
$$\mathbf{x_2} = \mathbf{x_0} + t_2 \mathbf{e_i} \tag{28b}$$

The fractional part of the front parameter for point $\mathbf{x_0}$ is:

$$\eta_f = \frac{|\mathbf{x_{10}}|}{|\mathbf{x_{12}}|} \tag{29}$$

where:

$$\mathbf{x_{10}} = \mathbf{x_0} - \mathbf{x_1} \tag{30a}$$
$$\mathbf{x_{12}} = \mathbf{x_2} - \mathbf{x_1} \tag{30b}$$

Finally the value of the front parameter is writes:

$$\eta = \eta_i + \eta_f \tag{31}$$

Parameter η is evaluated for every tip enriched node.

3.8.3 Front element shape functions

Shape functions of the linear front elements used in this work are linear 1D shape functions:

$$\mathbf{N}^g(\xi) = \begin{bmatrix} \frac{1-\xi}{2} & \frac{1+\xi}{2} \end{bmatrix} \tag{32}$$

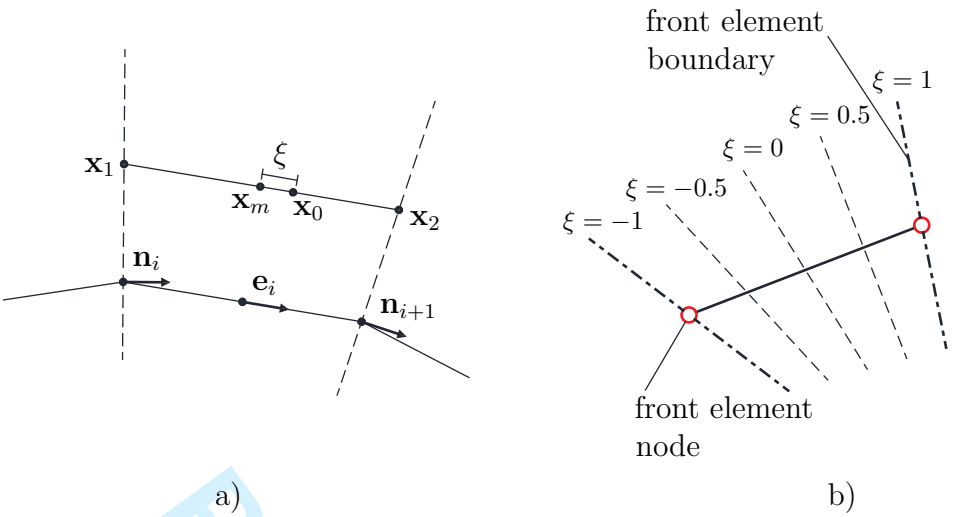

Fig. 17. Front element parameter for shape function evaluation.

where ξ is the local coordinate of the superimposed element.

The coordinate ξ is defined in a similar way to the fractional part of parameter η. The only difference being that while η_f assumes values form 0 to 1, ξ assumes values from -1 to 1 as illustrated in Figure 16.

The evaluation of ξ is almost identical to the evaluation of η_f:

$$\xi = \frac{2\ \mathbf{x_{12}} \cdot \mathbf{x_{m0}}}{|\mathbf{x_{12}}|^2} \tag{33}$$

where

$$\mathbf{x_{12}} = \mathbf{x_2} - \mathbf{x_1} \tag{34a}$$
$$\mathbf{x_{m0}} = \mathbf{x_0} - \mathbf{x_m} \tag{34b}$$
$$\mathbf{x_m} = \frac{\mathbf{x_1} + \mathbf{x_2}}{2} \tag{34c}$$

During the assembly procedure, the exact values of the ξ coordinate are used

rather than their FE approximation. This means that the above procedure has to be repeated for every Gauss point of every enriched element. In order to simplify the procedure, the nodal values of parameter η can be used to restrict the range of front elements that are checked for each Gauss point.

For the evaluation of shape function derivatives the derivatives of ξ with respect to the spatial coordinates are also needed. These can be calculated from the derivatives of the expressions given above. Further details about the assembly procedure used for the front elements are given in AppendixA.

4 Numerical examples

In this section numerical examples demonstrating the accuracy, convergence properties and computational cost of the proposed methodology are presented.

4.1 Implementation details

Some details regarding numerical integration and SIF evaluation will be given before presenting the benchmark problems solved.

4.1.1 Numerical integration

In XFEM in general and in the present methodology in particular, integration of enriched elements is of vital importance if optimal convergence and high accuracy are to be achieved. For elements containing the crack front, the approach used herein consists of combining the element partitioning algorithm proposed in Loehnert et al. [32] with a transformation as the one used in Minnebo [37] in order to integrate the singular tip enrichment functions as accurately as possible. For tip enriched elements that do not contain the crack front, a large number of Gauss points ($10 \times 10 \times 10$) was used and for jump enriched elements a simple element partitioning scheme as in Moës et al. [16] For the 2D examples, a similar approach was used utilizing almost polar integration ([23,24]) for elements containing the crack tip, a large number of Gauss points (20×20) for the rest of the tip elements and element partitioning for jump elements. Two attractive alternatives for numerical integration would be the methods of Natarajan et al. [54,36] and Chevaugeon et al. [38], however for the 3D case an extension of both methods would be required.

An additional difficulty that arises in the present work is the treatment of mesh interactions. More specifically, since enriched elements can be intersected by several front elements, those intersections should be appropriately taken into account by the numerical integration scheme in order to accurately integrate the enrichment functions and the front element shape functions. In the present work, the integration scheme described was used and element intersections

were ignored. This simplified strategy, which is similar to the one used in the s-finite element method [53], could introduce errors, thus there might be some room for improvement for the results presented in Section 4.

4.1.2 Integration of crack surface tractions

The contribution of the crack surface tractions in the final system of equations is obtained by substituting the displacement approximation of Equation 24 in the third integral of Equation 7. This integral is evaluated in an element wise fashion by locating the points where the crack faces and front intersect elements. The possible numbers of points are 3, 4 and 5 and the resulting surfaces to be integrated, which are assumed to be flat, are triangles, quadrilaterals and pentagons which are in turn divided into triangles. Those surfaces are moved by a negative and a positive increment along the direction of the level set gradient that is normal to the crack surface in order to obtain the upper and lower crack faces Γ^t_{c+} and Γ^t_{c-}. A large number of Gauss points (20×20 for quadrilaterals and 175 for triangles) was used to accurately integrate the surface integral.

4.1.3 Stress intensity factor estimation

For the evaluation of the SIFs an interaction integral was used. An additional term was added as in Walters et al. [55] in order to account for surface tractions applied at the crack faces:

$$I = -\int_V q_{i,j}\left(\epsilon^{\text{aux}}_{kl}\delta_{ij} - \sigma^{\text{aux}}_{kj}u_{k,i} - \sigma_{kj}u^{\text{aux}}_{k,i}\right)dV$$
$$-\int_V q_i\left(\sigma^{\text{aux}}_{kl,i}\epsilon_{kl}\delta_{ij} - \sigma_{kl}u^{\text{aux}}_{k,li} - \sigma^{\text{aux}}_{kl,l}u_{k,i}\right)dV - \int_{\Gamma^t_{c+}\cup\Gamma^t_{c-}}\left(t_j u^{\text{aux}}_{j,i}\right)q_i d\Gamma \quad (35)$$

where ϵ^{aux}, σ^{aux} and u^{aux} are the auxiliary stress, strain and displacement fields respectively which are defined as in Moës et al. [16] and t_j are the applied surface tractions. The additional term is integrated over the crack faces Γ^t_{c+} and Γ^t_{c-}.

Tensors in the above equation refer to a basis defined by the level set gradients as in Moës et al. [16]

4.1.3.1 Three dimensional domain integral For the 3D case the volume integrals of Equation 35 are evaluated in a parallelepiped mesh around each point of interest as in Moës et al. [16] and Sukumar et al [15]. Function q is also defined as in Sukumar et al [15].

Special attention has to be given to the evaluation of the third integral of Equation 35. In Walters et al. [55] a procedure is introduced to accurately integrate this term, in the present case however it is impossible to implement this procedure as the FE mesh does not conform to the crack geometry. The procedure used instead involves the detection of the points where the crack faces and front intersect elements of the parallelepiped mesh used in a similar manner to Subsection 4.1.2. The crack surfaces obtained this way are an

approximation of the FE surfaces in the SIF mesh. In order to make this approximation as accurate as possible, a large number of elements ($8 \times 8 \times 8$) is used for the SIF mesh. Moreover, since the surface integrals are important for the overall accuracy of the SIFs a large number of integration points, equal to the one used for the evaluation of the contribution of surface tractions, is employed.

The above procedure is both computationally expensive and of limited accuracy. Nevertheless, it is only used to provide an estimate of the accuracy of the SIFs computed by the proposed method. In the case where no surface tractions were present, a smaller number of elements could be used for the SIF mesh which would make the procedure faster.

4.1.3.2 Two dimensional domain integral For the 2D case the interaction integral is evaluated in a ring of elements around the crack tip and function q assumes a value of unity for nodes within a predefined distance from the crack tip and a value of zero for the rest of the nodes as in Moës et al. [14].

In addition, no surface tractions were considered so the third integral of Equation (35) vanishes. It should be noted however that in the 2D case a procedure similar to the one proposed by Walters et al. [55] would be possible to implement making the evaluation of this integral more accurate.

4.2 Benchmark problems

The energy and L_2 error norms used throughout this subsection are defined as follows, where it is noted that vectors and tensors are written in matrix form:

$$E = \left(\frac{\int_\Omega (\boldsymbol{\epsilon} - \boldsymbol{\epsilon}^h)^T \boldsymbol{D} (\boldsymbol{\epsilon} - \boldsymbol{\epsilon}^h) \, d\Omega}{\int_\Omega \boldsymbol{\epsilon}^T \boldsymbol{D} \boldsymbol{\epsilon} \, d\Omega} \right)^{1/2} \tag{36a}$$

$$L_2 = \left(\frac{\int_\Omega (\boldsymbol{u} - \boldsymbol{u}^h)^T (\boldsymbol{u} - \boldsymbol{u}^h) \, d\Omega}{\int_\Omega \boldsymbol{u}^T \boldsymbol{u} \, d\Omega} \right)^{1/2} \tag{36b}$$

where $\boldsymbol{\epsilon}$ and $\boldsymbol{u}$ are the strains and displacements obtained from the analytical solution and $\boldsymbol{\epsilon}^h$ and $\boldsymbol{u}^h$ are the corresponding numerically obtained values.

The two dimensional version of the method was implemented in Matlab while for the three dimensional version a C++ code was created utilizing the Gmm++ library [56] for linear algebra operations. For the solution of the systems of equations in the 3D examples the conjugate gradient (CG) solver of the Gmm++ package was employed in combination with a diagonal preconditioner. The convergence tolerance for the solver was set to 10^{-8}.

4.2.1 2D convergence study

The first problem considered in this section is also investigated in several other works and is usually employed in order to examine the convergence behavior of the numerous variations of the XFEM. It consists of an $L \times L$ square with an edge crack of length a, as depicted in Figure 17. The displacements

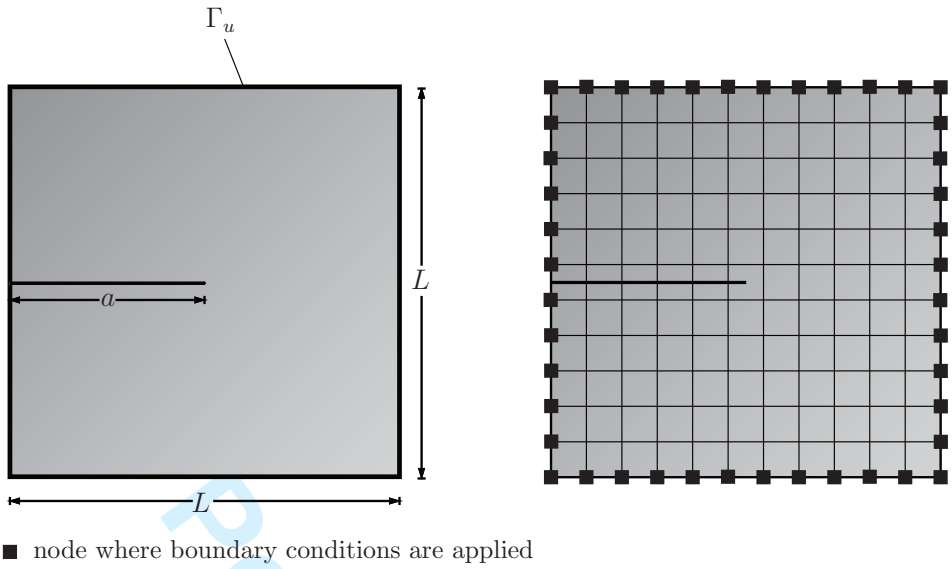

Fig. 18. Edge crack problem geometry and discretization. The boundary conditions are those provided by the Griffith crack problem so as to mimic the infinity of the domain. The dimensions of the problem are $L = 1$ unit, $a = 0.5$ units.

corresponding to the first term of the Williams expansion are imposed to the square as (Dirichlet) boundary conditions. The dimensions of the problem are taken as $L = 1$ unit, $a = 0.5$ units and the material parameters are $E = 100$ units and $\nu = 0.0$.

The domain is meshed using $n \times n$ linear quadrilateral elements where $n = 11, 21, 41, 61, 81, 101$. The problem is solved using both topological and geometrical enrichment. In the latter case an enrichment radius $r_e = 0.12$ units is used, this value was chosen so that for the 21×21 mesh a full layer of enriched elements is added. For this example the jump enrichment strategy of Subsection 3.4 is not used since displacements only consist of the first term of the Williams expansion.

Acronym	Description
FEM	The FE part of the approximation
XFEM	Standard XFEM
XFEMpm1	XFEM using dof gathering and point-wise matching
XFEMpm2	XFEMpm1 with the additional condition of subsection 3.5.2
GE-XFEM	XFEMpm2 with integral matching (Global Enrichment XFEM)

Table 1

List of acronyms used for the 2D convergence study.

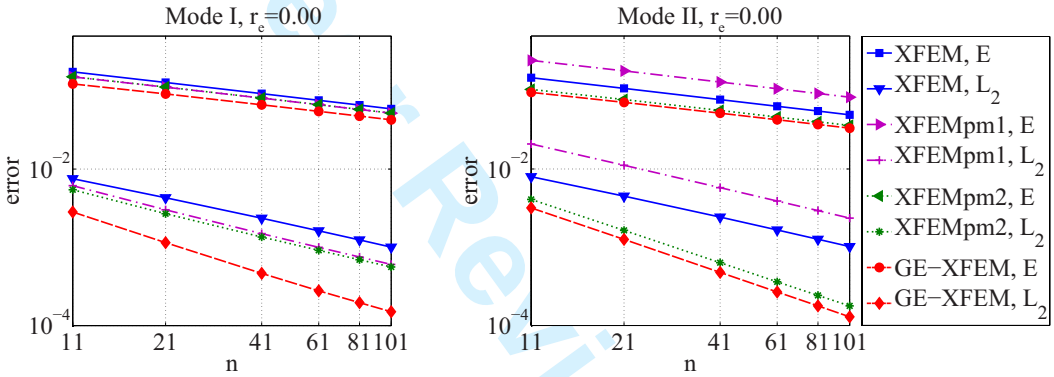

Fig. 19. Edge crack problem. L_2 and energy (E) norms versus the number of elements per side (n) for topological enrichment ($r_e = 0.00$ units) for modes I and II. The crack length is $a = 0.5$ units and the size of the domain is $L = 1$ unit. A description of the different methods mentioned in the figure is given in Table 1, while the corresponding convergence rates are given in Table 2.

The problem is solved for several variants of the method which are described in Table 1. For the second case (XFEMpm1) the additional condition of Subsection 3.5.2 is not imposed and the jump dofs of elements in contact to tip elements are treated as additional unknowns.

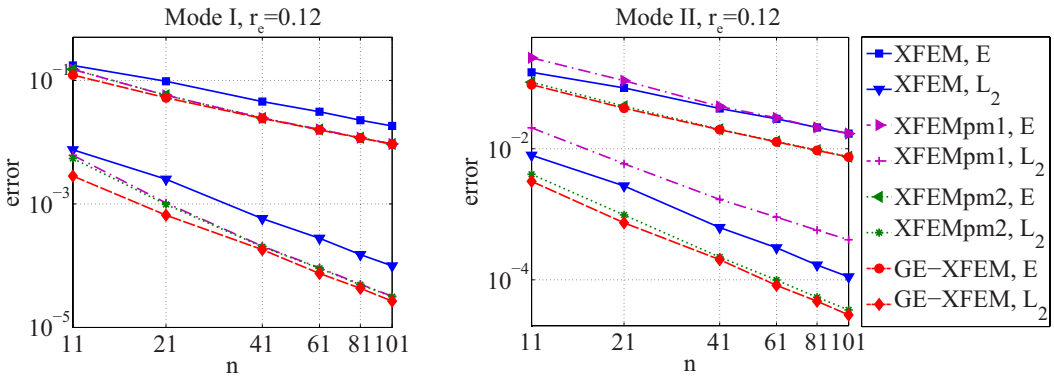

Fig. 20. Edge crack problem. L_2 and energy norms versus the number of elements per side (n) for geometrical enrichment with an enrichment radius $r_e = 0.12$ units for modes I and II. The crack length is $a = 0.5$ units and the size of the domain is $L = 1$ unit. A description of the different methods mentioned in the figure is given in Table 1, while the corresponding convergence rates are given in Table 2.

4.2.1.1 L_2 and energy norms In Figures 18 and 19 the $L2$ and Energy error norms are depicted for Mode I and II fracture, for topological and geometrical enrichment for four cases. In Table 2 the convergence rates for all the above cases are given.

It can be noted from Figures 18 and 19 that the additional point-wise matching condition significantly improves results for Mode II cracks. More specifically, the application of the additional constraint decreases errors by more than 75% for the L_2 norm and more than 50% for the energy norm. Moreover, integral matching mostly influences Mode I cracks when topological enrichment is used while it improves results only slightly for the rest of the cases. The final curves achieved (GE-XFEM) provide significant improvement compared to standard XFEM since for all the cases examined the errors for the proposed method

	$r_e = 0.00$		$r_e = 0.12$	
	Mode I	Mode II	Mode I	Mode II
XFEM E	0.491	0.493	1.030	0.982
XFEM L_2	0.908	0.928	1.980	1.955
XFEMpm1 E	0.483	0.489	1.243	1.211
XFEMpm1 L_2	1.044	0.984	2.355	1.773
XFEMpm2 E	0.483	0.479	1.245	1.179
XFEMpm2 L_2	1.022	1.414	2.311	2.151
GE-XFEM E	**0.477**	**0.476**	**1.156**	**1.140**
GE-XFEM L_2	**1.326**	**1.446**	**2.086**	**2.100**

Table 2

Edge crack problem. Convergence rates for the curves of Figures 18 and 19 for the energy (E) and L_2 norms for topological ($r_e = 0.00$ units) and geometrical ($r_e = 0.12$ units) enrichment. Note the superconvergence property of the global enrichment approach in the L_2 norm. The method is slightly suboptimal in the energy norm.

were reduced by more than 50% for the L_2 norm and 25% for the energy norm.

Moreover, it is interesting to note that for all the cases considered, the global enrichment approach provides similar convergence rates and lower errors than standard XFEM while also reducing the number of enriched dofs. We will see in the following that this advantage is compounded by the fact solution times are reduced considerably thanks to the improved conditioning of the system matrices.

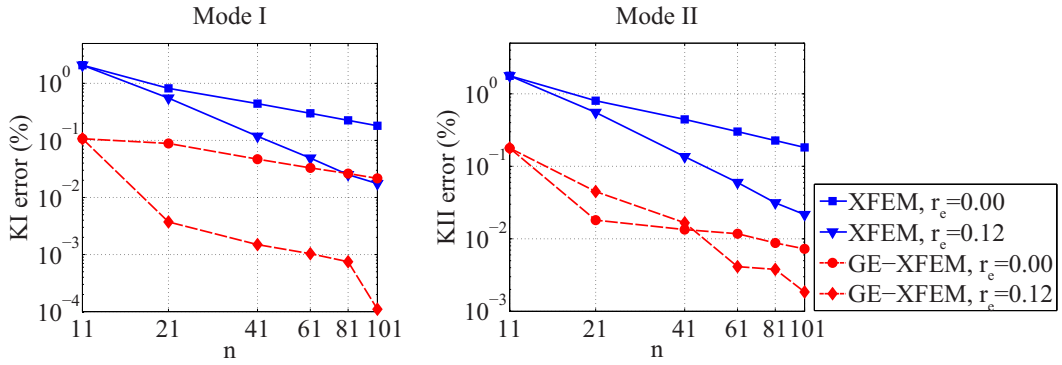

Fig. 21. Edge crack problem. Mode I and II stress intensity factors predicted by XFEM and GE-XFEM versus the number of elements per side (n) for topological ($r_e = 0.00$ units) and geometrical ($r_e = 0.12$ units) enrichment. The crack length is $a = 0.5$ units and the size of the domain is $L = 1$ unit. The convergence rates for all cases are given in Table 3.

	$r = 0.00$		$r = 0.12$	
	Mode I	Mode II	Mode I	Mode II
XFEM	1.071	1.005	2.195	2.021
GE-XFEM	0.759	1.246	2.545	2.029

Table 3

Edge crack problem. Convergence rates for the SIFs of Figure 20.

4.2.1.2 Stress Intensity Factors Stress intensity factors of the proposed method and standard XFEM are compared in Figure 20, convergence rates for all cases are given in Table 3. A radius $r_d = 0.15$ is used for SIF evaluation.

In the results produced by the proposed method some fluctuations occur which were also observed in Laborde et al. [23].Nevertheless, despite the fluctuations, the accuracy is substantially improved and the convergence rates are similar to standard XFEM. It should be noted that the convergence rates of the

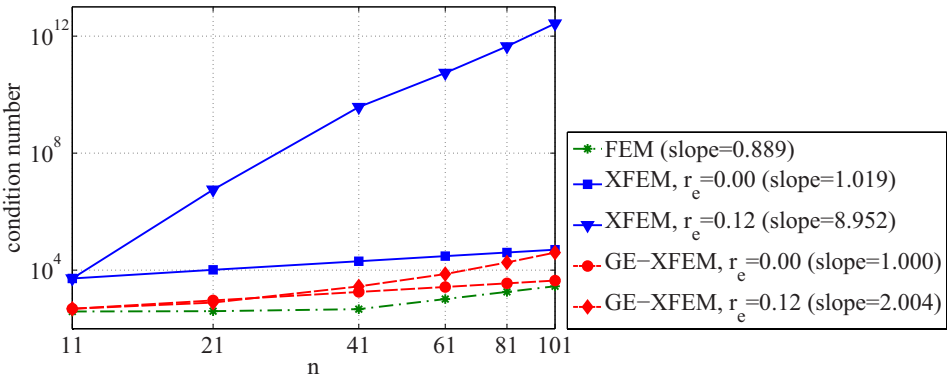

Fig. 22. Edge crack problem. Condition numbers of the system matrices produced by XFEM and GE-XFEM versus the number of elements per side (n) for topological ($r_e = 0.00$ units) and geometrical ($r_e = 0.12$ units) enrichment. The crack length is $a = 0.5$ units and the size of the domain is $L = 1$ unit. Condition numbers of the FE part of the approximation are also plotted for reference.

computed SIFs for this example are almost equal to the convergence rates obtained for the displacements (L_2 norm).

4.2.1.3 Conditioning In Figure 21 the condition numbers for standard XFEM and the proposed method are illustrated. The condition numbers of the FE part of the corresponding matrices are also plotted. The proposed method performs significantly better than standard XFEM in every case. When topological enrichment is used condition numbers corresponding to the global enrichment approach are one order of magnitude lower than standard XFEM and increase in a similar rate, while for the geometrical enrichment case the rate of increase is reduced by 4 times resulting in condition numbers several orders of magnitude lower. Furthermore, when geometrical enrichment is used,

condition numbers of the proposed method change only slightly compared to topological enrichment, and for the cases considered are even smaller than the ones corresponding to standard XFEM for the topological enrichment case.

4.2.2 3D convergence study

The accuracy and convergence properties of the proposed method for the general 3D case are demonstrated through a novel benchmark problem. This problem is based on the analytical solution for the problem of a penny crack in an infinite solid subjected to uniform normal and shear loading [57]. Full displacement and stress fields are available for this problem [57], which makes possible the evaluation of L_2 and energy error norms.

The displacement fields provided by the analytical solution are imposed as constraints along the boundaries of the domain considered as in the 2D convergence study. In addition, a uniform normal or shear load has to be applied on the crack faces.

The proposed benchmark differs from the one used in 2D convergence studies in several ways:

- Firstly, it includes the full solution for the whole crack, rather than only the first term of the Williams expansion for a small part of the crack around the crack front. Thus, the effects of higher order terms and most importantly of the size of the enriched area in the accuracy of the various

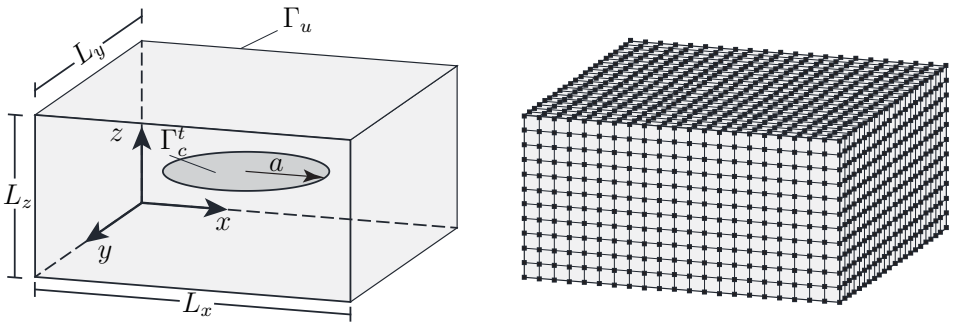

Fig. 23. Penny crack problem geometry and discretization. The boundary conditions provided by the analytical solution are imposed along the boundaries of the domain. Uniform normal and shear loads are applied to the crack surfaces. The dimensions of the problem are $L_x = L_y = 2L_z = 0.4$ units and $a = 0.1$ unit.

methods can be investigated.

- Secondly, the proposed problem involves variation of the solution parameters (e.g. SIFs) across the length of the crack front. This feature is important both for the general case where a three dimensional behavior is preferable, and for the present case where the effectiveness of the superimposed element approach needs to be studied.

- Furthermore, the crack front considered is curved which is the case in practical applications ([18,19,20,21,22]).

For the above reasons, the proposed benchmark should provide a reliable means of testing the accuracy of computational fracture methods in general, and of the proposed method in particular.

Acronym	Description
XFEM	Standard XFEM
GE-XFEM	The proposed method (Global Enrichment XFEM)
GE-XFEM1	The proposed method without the enrichment strategy of subsection 3.4

Table 4

List of acronyms used for the 3D convergence study.

A parallelepiped domain is considered with dimensions $L_x \times L_y \times L_z$. with a penny crack of radius a as in Figure 22. The dimensions of the problem were set to $L_x = L_y = 2L_z = 0.4$ units and $a = 0.1$ unit. A uniform normal and a uniform shear load of magnitude 1 are applied at the crack faces (mixed mode loading). The material parameters used are $E = 100$ units and $\nu = 0.3$.

The domain is meshed using several meshes consisting of $n_x \times n_y \times n_z$ hexahedral elements where $n_x = n_y = 2n_z = n$ and $n \in \{21, 41, 61, 81, 101\}$.

The acronyms used for the different methods tested are described in Table 4.

4.2.2.1 L_2 and energy norms In Figure 23 the influence of the crack front mesh on the accuracy of the results is investigated for two different enrichment radii ($r_e = 0.00$ and $r_e = 0.02$) and for a mesh consisting of $31 \times 61 \times 61$ elements. The crack front meshes used consist of $n_f = 4, 8, 16, 32, 64, 128$ elements. Despite the fact that the solution parameters vary significantly along the crack front, the influence of the front mesh density is minimal. More precisely, for all the discretizations except the first two (4 and 8 front elements)

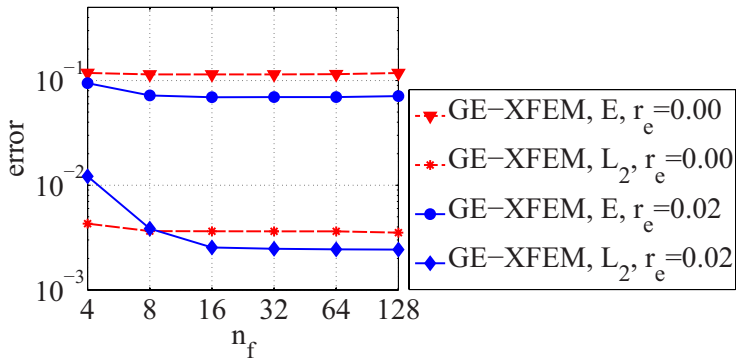

Fig. 24. Penny crack problem. Influence of the crack front mesh density (n_f is the number of elements along the front) in the energy (E) and L_2 norms for the proposed method for topological ($r_e = 0.00$ units) and geometrical enrichment with an enrichment radius $r_e = 0.02$ units. The radius of the crack is $a = 0.1$ units and the size of the domain is $L_x = L_y = 2L_z = 0.4$ units. Results refer to a mesh consisting of $31 \times 61 \times 61$ elements.

the difference is less than 5% in the L_2 norm. A possible explanation for the above situation is the fact that the interactions of the two meshes are ignored during numerical integration as mentioned in subsection 4.1.1, consequently for a more accurate numerical integration scheme a different behavior could occur. For the following examples 32 elements were used for the $11 \times 21 \times 21$ and $21 \times 41 \times 41$ meshes and 64 elements for the rest.

Next, the influence of the enrichment radius r_e on the accuracy of the results is examined. As already mentioned in Subsection 3.4, standard XFEM compensates for higher order terms by allowing spatial variation of the coefficients of the enrichment functions. The proposed method does not allow any variation in the plane normal to the crack front, as a result when larger enrichment radii

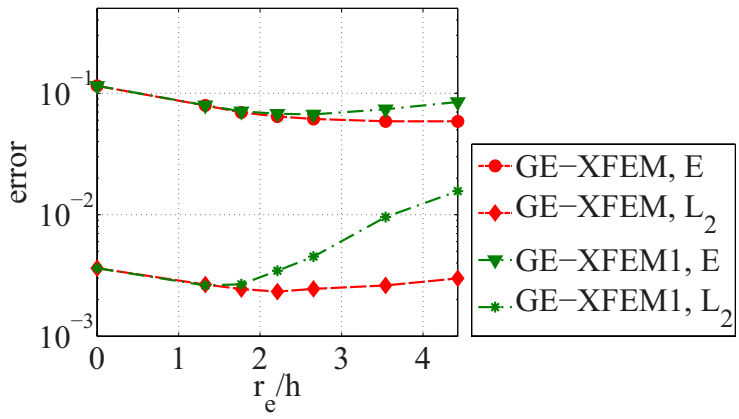

Fig. 25. Penny crack problem. Influence of the enrichment radius (r_e) in the energy (E) and L_2 norms for two variations of the proposed method described in Table 4. The radius of the crack is $a = 0.1$ units and the size of the domain is $L_x = L_y = 2L_z = 0.4$ units. Results refer to a mesh consisting of $31 \times 61 \times 61$ elements. h is the mesh parameter.

are used a loss of accuracy occurs. The situation is improved by employing the enrichment strategy of Subsection 3.4, however as the enrichment radii and the layers of enriched elements around the crack front increase, some loss of accuracy in the displacements is still observed. The situation is illustrated in Figure 24 where L_2 and energy norms are plotted against the enrichment radius r_e divided by the mesh parameter h since it was observed that the loss of accuracy occurs when a certain number of layers of enriched elements is added, rather than at some fixed value of the enrichment radius. Figure 24 refers to the $31 \times 61 \times 61$ mesh.

Energy and L_2 norms are shown in Figures 25 and 26 for four different cases: topological enrichment ($r_e = 0.00$), topological enrichment with a fixed num-

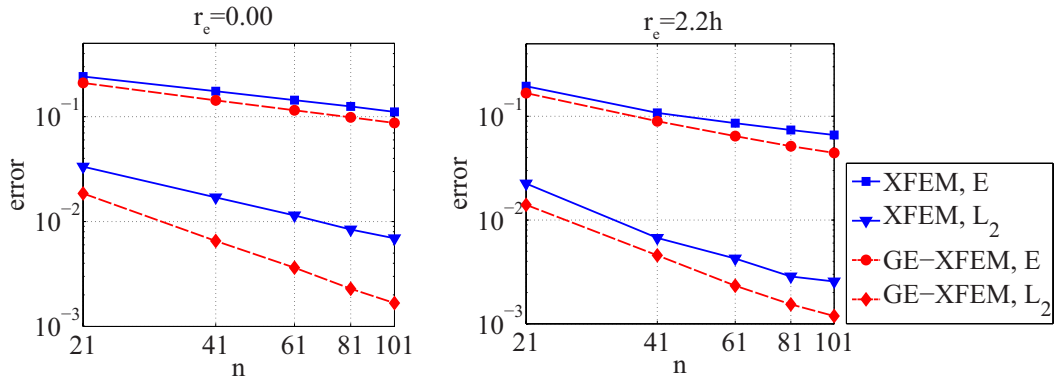

Fig. 26. Penny crack problem. L_2 and energy (E) norms versus the number of elements along the largest sides (n) for topological enrichment ($r_e = 0.00$ units and $r_e = 2.2h$) for mixed mode loading. The radius of the crack is $a = 0.1$ units and the size of the domain is $L_x = L_y = 2L_z = 0.4$ units. A description of the different methods mentioned in the figure is given in Table 4, while the corresponding convergence rates are given in Table 5.

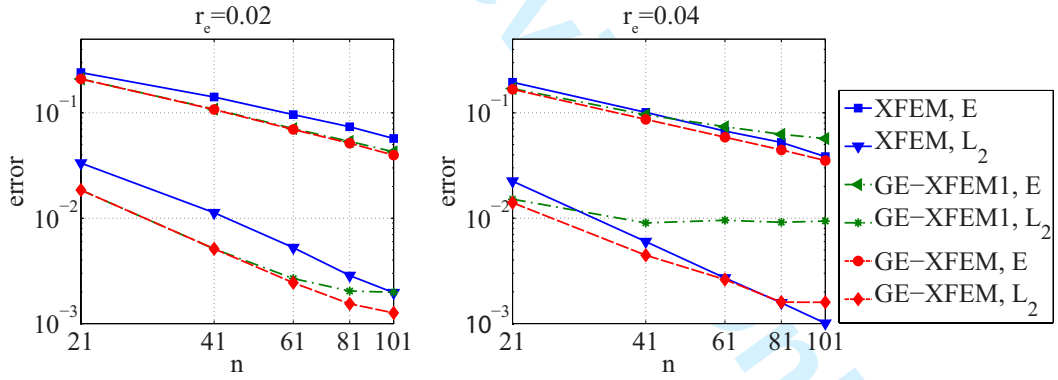

Fig. 27. Penny crack problem. L_2 and energy (E) norms versus the number of elements along the largest sides (n) for geometrical enrichment with enrichment radii $r_e = 0.04$ units and $r_e = 0.04$ units for mixed mode loading. The radius of the crack is $a = 0.1$ units and the size of the domain is $L_x = L_y = 2L_z = 0.4$ units. A description of the different methods mentioned in the figure is given in Table 4, while the corresponding convergence rates are given in Table 5.

	$r_e = 0.00$	$r_e = 2.2h$	$r_e = 0.02$	$r_e = 0.04$
XFEM E	0.492	0.686	0.911	1.015
XFEM L_2	1.009	1.405	1.824	1.976
GE-XFEM1 E	-	-	1.016	0.706
GE-XFEM1 L_2	-	-	1.481	0.289
GE-XFEM E	**0.558**	**0.850**	**1.057**	**0.988**
GE-XFEM L_2	**1.535**	**1.594**	**1.753**	**1.448**

Table 5

Penny crack problem. Convergence rates for the curves of Figures 25 and 26 for the energy (E) and L_2 norms for topological ($r_e = 0.00$ and $r_e = 2.2h$) and geometrical ($r_e = 0.02$ units and $r_e = 0.04$ units) enrichment. It is observed that when the proposed enrichment strategy is not used (GE-XFEM1) convergence rates deteriorate significantly.

ber of layers of enriched elements ($r_e = 2.2h$) and geometrical enrichment with enrichment radii $r_e = 0.02$ and $r_e = 0.04$, the respective convergence rates are given in Table 5. For the second case the enrichment radius was set to the value which yielded the best results in terms of displacements, this value was obtained from Figure 24 where it is observed than when the enrichment radius becomes larger than the aforementioned value, the L_2 error norm starts to increase. It can be observed that the proposed method performs better than standard XFEM for almost all cases. Additionally, the proposed enrichment strategy substantially improves results, especially as the enrichment radius used increases. However, it should be noted that the behavior observed for

the larger enrichment radius ($r_e = 0.04$) will also occur for the smaller one ($r_e = 0.02$) for denser meshes, where the enrichment radius is larger than the "optimal" value observed ($2.2h$), leading to loss of accuracy. This behavior, which affects mostly displacements, can be attributed to the lack of spatial variability of the coefficients of the enrichment functions and can be regarded as a drawback of the dof gathering approach. A possible solution would be the introduction of some spatial variability to the tip enrichment functions which would not deteriorate conditioning significantly. Such a solution would be possible within the framework of the proposed method, nevertheless it will not be considered since it would exceed the scope of the present work which is mostly to provide a means to extend dof gathering to 3D fracture problems.

4.2.2.2 Stress Intensity Factors Stress intensity factors were computed for several of the above cases. In Figures 27 and 28 errors in the SIFs are illustrated as functions of the angle θ for two different meshes ($21 \times 41 \times 41$ and $41 \times 81 \times 81$) for topological ($r_e = 0.00$) and geometrical ($r_e = 0.02$) enrichment. Due to symmetry only the values for $0° \leq \theta \leq 90°$ are presented. A virtual extension domain of dimensions $r_1 = 3h, r_2 = 3h, r_3 = h$ was used in the calculations.

It is observed that although the errors are quite small, it is not possible to obtain a convergence behavior like thse of Subsection 4.2.1.2 for the 2D case. More specifically, although errors decrease slightly with mesh refinement for

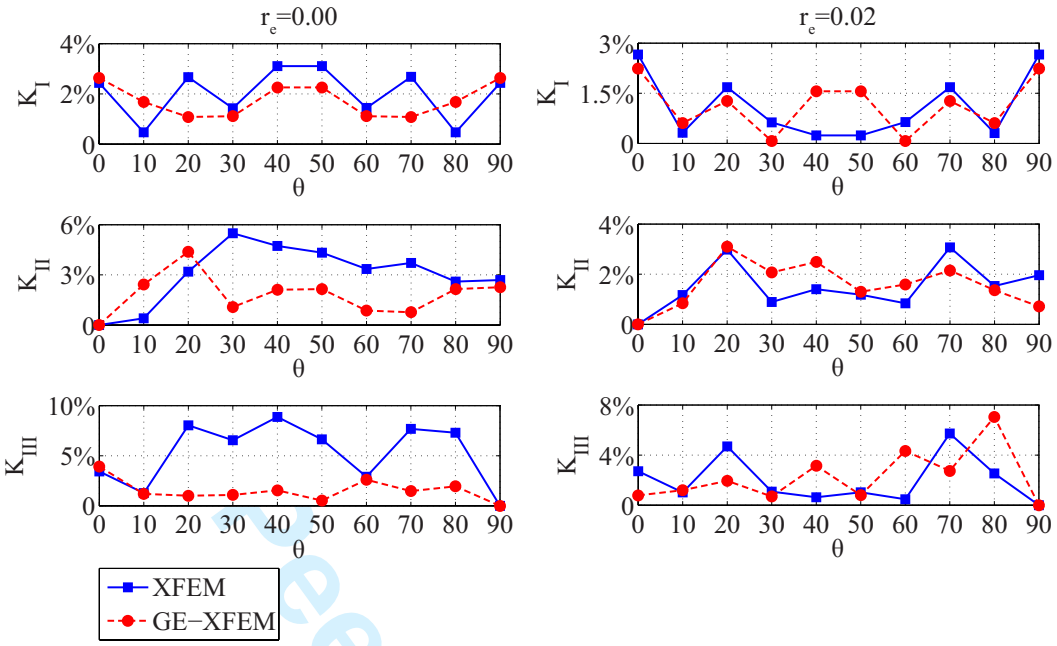

Fig. 28. Penny crack problem. Comparison of the mode I, II and III stress intensity factors predicted by XFEM and GE-XFEM for topological ($r_e = 0.00$ units) and geometrical ($r_e = 0.02$ units) enrichment for the $21 \times 41 \times 41$ mesh. The radius of the crack is $a = 0.1$ units and the size of the domain is $L_x = L_y = 2L_z = 0.4$ units.

most points, this accuracy improvement is not comparable to that of the 2D case. In addition, for some points along the crack front (for instance $\theta = 80°$ for Mode III) errors increase for finer meshes.

The above behavior can be associated to the interpolation and integration errors introduced by the use of the SIF mesh, as discussed also in subsection 4.1.3.1. An additional cause could be the fact that in the evaluation of the interaction integral, the curvature of the crack front is ignored [58]. It should also be noticed that problems in the extraction of SIFs for the 3D case have also been observed for standard finite elements [59].

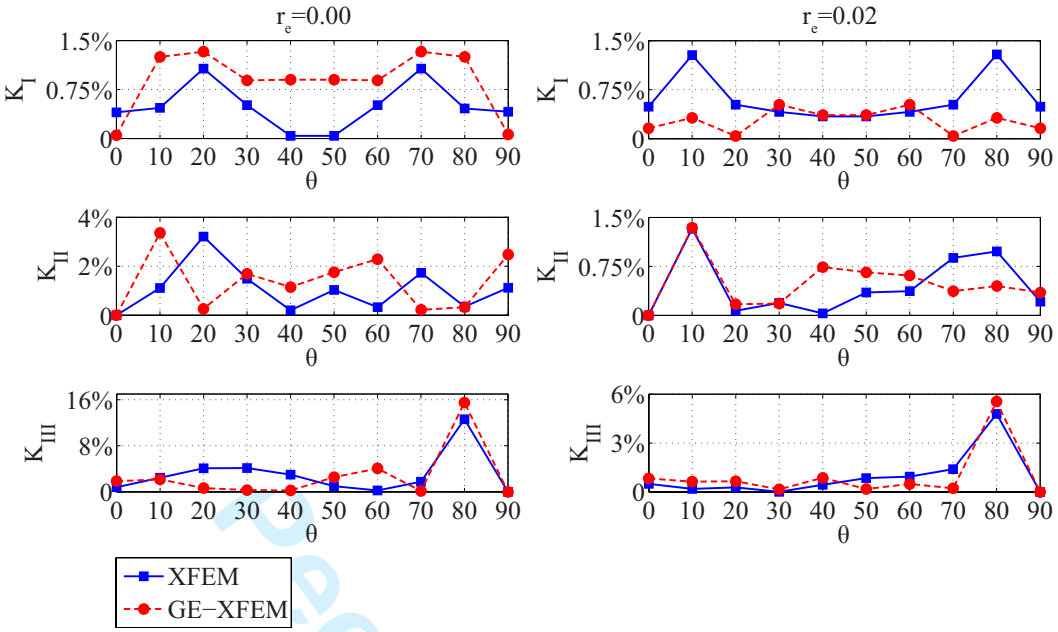

Fig. 29. Penny crack problem. Comparison of the mode I, II and III stress intensity factors predicted by XFEM and GE-XFEM for topological ($r_e = 0.00$ units) and geometrical ($r_e = 0.02$ units) enrichment for the $41 \times 81 \times 81$ mesh. The radius of the crack is $a = 0.1$ units and the size of the domain is $L_x = L_y = 2L_z = 0.4$ units.

Finally, although it is not possible to get an accurate estimate, the accuracy of the SIFs predicted by the proposed method is similar to the one provided by standard XFEM. A more accurate SIF evaluation procedure, which is the subject of future work, however would provide better insight.

4.2.2.3 Conditioning In this section the conditioning of the system matrices produced by the proposed method is tested and compared to standard XFEM for the general 3D case. Instead of evaluating the condition numbers of the system matrices, the number of iterations required by the solver to reach the predefined tolerance (10^{-8}) is used as an estimate, this approach has the

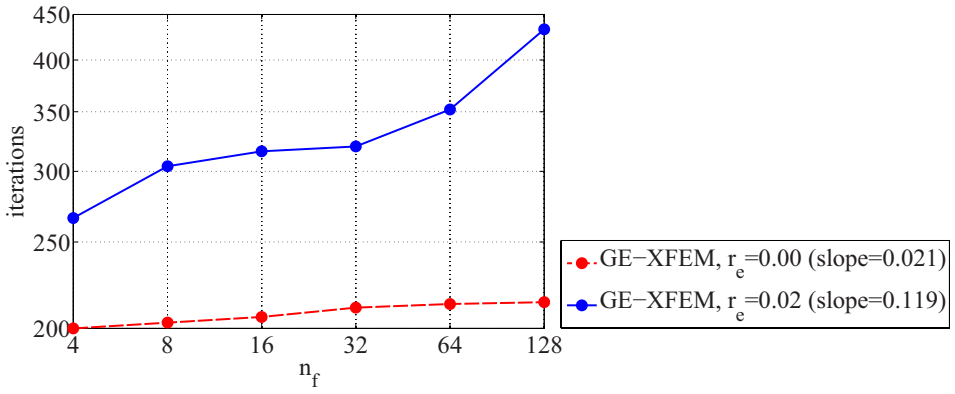

Fig. 30. Penny crack problem. Influence of the crack front mesh density (n_f is the number of elements along the front) in the number of iterations required to solve the system of equations produced by the proposed method for topological ($r_e = 0.00$ units) and geometrical enrichment with an enrichment radius $r_e = 0.02$ units. The radius of the crack is $a = 0.1$ units and the size of the domain is $L_x = L_y = 2L_z = 0.4$ units. Results refer to a mesh consisting of $31 \times 61 \times 61$ elements.

additional advantage of providing also a comparison of the time needed to solve the resulting system of equation for each method since solution times are dominated by the conjugate gradient iterations. It should be noted that the following figures refer to the number iterations required by a conjugate gradient solver with a diagonal preconditioner.

The number of iterations required for the $31 \times 61 \times 61$ mesh for different numbers of front elements is given in Figure 29 in order to estimate the influence of the front mesh density in conditioning. It can be noted that the number of iterations required increases as the front mesh is refined when geometrical enrichment is used but remains fairly unaffected for topological enrichment.

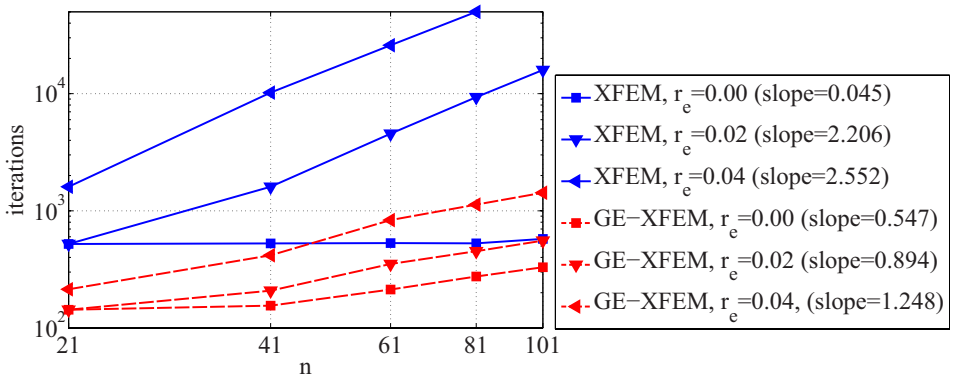

Fig. 31. Penny crack problem. Number of iterations required to solve the system of equations produced by XFEM and the proposed method versus the number of elements along the largest sides (n) for three different enrichment radii: $r_e = 0.00$ units (topological enrichment), $r_e = 0.02$ units and $r_e = 0.04$ units (geometrical enrichment). The radius of the crack is $a = 0.1$ units and the size of the domain is $L_x = L_y = 2L_z = 0.4$ units. The proposed method reduces the required number of iterations in every case.

In Figure 30 the number of iterations required by the CG solver for XFEM and the proposed method for topological and geometrical enrichment is presented. Again, the number of iterations required by the proposed method is significantly reduced. In fact, for the smaller enrichment radius used ($r_e = 0.02$) the number of iterations for the proposed method is even smaller than the one required for XFEM with topological enrichment. Another important fact is that even for topological enrichment the proposed method requires a significantly smaller number of iterations than XFEM. For example, in the $51 \times 101 \times 101$ mesh, where the difference is the smallest, standard XFEM requires 573 iterations versus 330 for the proposed method. In addition, for the larger enrich-

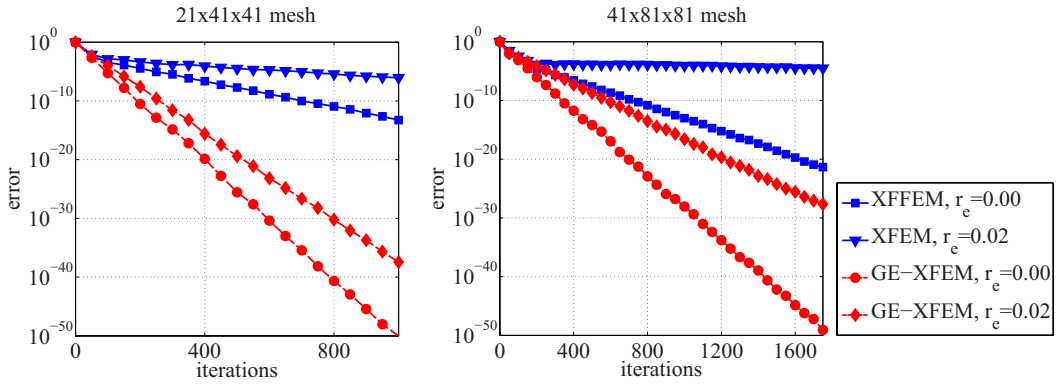

Fig. 32. Penny crack problem. Comparison of the performance of the PCG solver for XFEM and the proposed method. Results are shown for two different meshes consisting of $21 \times 41 \times 41$ and $41 \times 81 \times 81$ elements. Both topological ($r_e = 0.00$ units) and geometrical enrichment ($r_e = 0.02$ units) are considered.

ment radius ($r_e = 0.04$) the systems produced by XFEM are almost unsolvable as they require more than 50,000 iterations for the two denser meshes ($41 \times 81 \times 81$ and $51 \times 101 \times 101$) while the proposed method converges after a far smaller number of iterations (less than 1,500 for both cases). As far as the rates of increase are concerned, the change in the number of front elements used is probably the reason why the proposed method presents a larger rate of increase for topological enrichment. For the two cases of geometrical enrichment studied, the rates of increase are reduced by a factor of 2 compared to standard XFEM.

As an additional means to assess the conditioning of the system matrices, the error achieved by the solver after different iterations is calculated as in Menk and Bordas [26] and presented in Figure 31 for topological and geometrical enrichment and two different meshes. Again, it can be deduced that the CG

Mesh	FE dofs	XFEM dofs ($r_e = 0.00$)	XFEM dofs ($r_e = 0.02$)	XFEM dofs ($r_e = 0.04$)	GE-XFEM dofs
$11 \times 21 \times 21$	17,424	2,232	2,232	5,856	696
$21 \times 41 \times 41$	116,424	5,376	11,904	42,288	1,920
$31 \times 61 \times 61$	369,024	9,456	37,752	137,280	4,464
$41 \times 81 \times 81$	847,224	14,424	84,696	320,664	7,512
$51 \times 101 \times 101$	1,623,024	20,376	162,528	620,184	11,544

Table 6

Penny crack problem. Comparison of the total number of enriched dofs added by XFEM and the proposed method for topological ($r_e = 0.00$ units) and geometrical enrichment($r_e = 0.02$ units and $r_e = 0.04$ units). FE dofs is the number of regular dofs. Note that for the proposed method the number of additional unknowns is independent of the enrichment radius (r_e).

solver converges much faster for the proposed method in every case.

4.2.2.4 Number of enriched degrees of freedom For 2D problems the number of additional unknowns is usually negligible compared to the total number of unknowns. For 3D problems however, the additional unknowns associated to the enriched part of the approximation could significantly increase the total number of degrees of freedom. For this reason the number of enriched dofs added by the proposed method is considered in this section.

In Table 6 a comparison is made between the total number of enriched dofs (both jump and tip) added by standard XFEM and the proposed approach

for the cases examined in the previous subsections. In contrast to standard XFEM, the number of additional unknowns for the global enrichment approach is completely independent of the enrichment radius. Additionally, the total number of enriched dofs for the proposed method is reduced by 45% to more than 98% depending on the mesh and enrichment radius. Finally, and most important, the increase in the total number of unknowns for standard XFEM ranges from less than 1.5% to almost 40% while for the proposed method this increase never exceeds a percentage of 4%. Thus the additional cost and memory requirements are minimized by the global enrichment approach.

It should be noted that the dof numbers given above as well as the numbers of iterations given in the previous subsections refer to the specific problem examined and will vary for different problems depending on the size of the crack and/or length of the crack front relative to the domain considered. Nevertheless, although the rate decrease in the computational cost might change for different problems, the proposed method will always be computationally advantageous when compared to XFEM since the number of additional unknowns will always be smaller and unaffected by changes in the enrichment radius and the conditioning of the system matrices will always be improved as a result of dof gathering.

5 Conclusions

A method was described which enables the use of global enrichment functions for the extended finite element method. The method is almost always more accurate than standard XFEM for a much reduced computational expense. This efficiency is attributed to the use of much fewer enriched degrees of freedom and a much improved conditioning of the system matrices.

The method relies on the principles introduced in the works of Laborde et. al. [23] and Chanine et al. [47] in conjunction with a novel form of enrichment in order to obtain some of the advantages of the two dimensional method in the general three dimensional case. Although only plane cracks are treated in the examples presented this work, the method is also applicable to more general crack geometries.

A benchmark problem was proposed for testing numerical fracture methods which enables the computation of L_2 and energy error norms for the general 3D case. The accuracy of the proposed global enrichment approach was tested and compared to that of standard XFEM through the above benchmark problem.

From the above, it results that the proposed approach provides several advantages. When topological enrichment is used it produces more accurate results than the standard method requiring smaller solution times. Moreover, it makes

possible the application of geometrical enrichment in 3d applications without the use of special preconditioners, since it produces system matrices with significantly improved conditioning compared to standard XFEM. In terms of assembly time, the proposed method is also faster than standard XFEM because of the reduced number of shape functions evaluated for each element.

One possible drawback of the method is that, when the number of enriched elements around the crack front exceeds a certain value, the error in the displacements increases. Also, the method is not straightforward to implement in existing XFEM codes. Finally, the additional point wise-matching constraints introduced might be quite complex to implement for higher order elements.

Some directions of future work include:

- The improvement of the method in order to minimize the loss of accuracy observed for large enrichment radii.
- The use of improved SIF evaluation [58] methods in order to better asses the accuracy of the predicted SIFs.
- The combination of the method with goal oriented a posteriori error estimators [42,43,44,45,46] and local front mesh and FE mesh refinement in order to further improve the accuracy of the method.
- The application of the method to crack propagation problems through the use of different crack representation methods [16,17,48,49,50].

A Assembly of the front elements

Since the assembly of the stiffness matrices is done in an element wise manner and finite elements will be usually intersected by several front elements, the interactions between the two meshes have to be specified. In more detail, for every tip enriched element the corresponding front elements and dofs, i.e. the front elements that intersect this element and the dof numbers of their nodes, have to be determined. This can be easily achieved by employing the front parameter η.

Once the front parameter has been evaluated for every node of a given element and since the numbering of front elements and nodes is continuous, it is possible to associate elements of the two meshes. The association of the two meshes is done employing the minimum and maximum value of the front parameter for each element and a mapping between the nodal numbers of the two meshes, these concepts are described next.

A.1 Minimum and maximum value of the front parameter

The minimum and maximum nodal values of the integer part of the front parameter η_i are found (η_{min} and η_{max}) for a given element. All front elements with numbers in the range between those two values are intersected by the element. For closed cracks however, there might be cases where the above

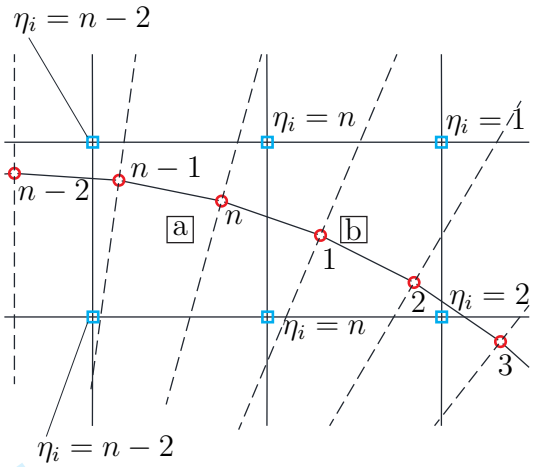

Fig. A.1. Front element parameter for shape function evaluation.

statement does not hold. In particular, if a closed crack front discretized with n elements is considered as in Figure A.1, although elements in the vicinity of the first front node will have a minimum value close to unity and a maximum value close to n, front elements within that range will not be intersected.

Elements falling in the case described above can be detected by defining a number $n_t < n$ and performing the following checks:

$$\eta_{min} \leq n_t \tag{A.1a}$$
$$\eta_{max} \geq n - n_t \tag{A.1b}$$

If those conditions are both true, the minimum and maximum values are interchanged. The range of front element numbers intersected by the element in this case is from η_{max} to n and from 1 to η_{min}.

The value of n_t is an estimate of the maximum number of front elements that could intersect any given finite element and should be defined by taking into

account the relation between the mesh parameter and the length of the front elements. For curved crack fronts, the value of the enrichment radius should also affect the choice of that value.

For the case of Figure A.1, the above would mean that while the initial values for element b would be $\eta_{min} = 2$ and $\eta_{max} = n$, those values would have to be interchanged so that $\eta_{min} = n$ and $\eta_{max} = 2$.

A.2 Local to global and global to local dof mapping

Using the above information, the number of enriched dofs for any tip enriched element can be computed. In addition, mappings between local and global dof numberings can be defined:

$$i_g = \begin{cases} i_l + \eta_{min} - 1, & i_l \leq n - \eta_{min} \\ i_l - n + \eta_{min} - 1, & i_l > n - \eta_{min} \end{cases} \tag{A.2a}$$

$$i_l = \begin{cases} i_g - \eta_{min} + 1, & i_g \geq \eta_{min} \\ i_g + n - \eta_{min} + 1, & i_g < \eta_{min} \end{cases} \tag{A.2b}$$

Applying the above relations to the case of Figure A.1 it can be easily found that for element b, where $\eta_{min} = n$ and $\eta_{max} = 2$, the first associated front node ($i_l = 1$), is node n ($i_g = n$). Conversely, front node 2 ($i_g = 2$) is the 3rd node ($i_l = 3$) associated with element b.

A.3 Shape function evaluation and assembly procedure

Mappings of Equations A.2 are used in two occasions during the assembly process.

Since every tip element is associated with several front elements, the enriched parts of its shape functions are matrices of corresponding dimensions. Each Gauss point however, is only associated with one front element, and the enriched shape functions evaluated at that point are matrices with dimensions corresponding to two front nodes. In order to place the enriched shape functions of every Gauss point in the correct position of the matrix corresponding to the whole element, the integer part of the front parameter is evaluated and the global to local mapping is used to obtain the correct location.

During the assembly of element matrices, the global front node numbers associated with every element have to be known. For this purpose, the local to global mapping is employed.

The shape function evaluation and assembly procedure for the enriched part of the stiffness matrix for a given element can be summarized in the following steps:

(1) **Minimum and maximum value of front parameter.**

The minimum and maximum values of the front parameter are found

as described in subsection A.1

(2) **Number of enriched dofs.**

Using the minimum and maximum values of the front parameter, the number of enriched dofs for the given element is found.

(3) **Shape function and stiffness matrix size.**

Using the number of enriched dofs the size of the shape functions and of the enriched part of the stiffness matrix are found.

(4) **Numerical integration/Shape function evaluation.**

During the numerical integration the enriched shape functions are evaluated for each Gauss point. The global to local mapping is employed to place individual Gauss point shape functions in the correct location in the element shape function.

(5) **Assembly.**

Once the stiffness of an individual element is computed, the corresponding global dof numbers can be obtained using the local to global mapping.

Finally, as far as computational effort is concerned, since in the majority of cases a tip enriched finite element should not be associated with more than three or four front nodes and since every integration point is only associated with two nodes, the number of shape function evaluations for each Gauss point is significantly reduced compared to standard XFEM, resulting in reduced assembly times.

Acknowledgements

Eleni Chatzi would like to acknowledge the support of the Swiss National Science Foundation (SNSF) under Research Grant, Project # 200021-153379.

Also Stéphane P. A. Bordas would like to thank partial funding for his time provided by the EPSRC under grant EP/G042705/1 Increased Reliability for Industrially Relevant Automatic Crack Growth Simulation with the eXtended Finite Element Method as well as the European Research Council Starting Independent Research Grant (ERC Stg grant RealTcut, agreement No. 279578) entitled Towards real time multiscale simulation of cutting in non-linear materials with applications to surgical simulation and computer guided surgery.

References

[1] OC Zienkiewicz, RL Taylor, and JZ Zhu. *The Finite Element Method: its Basis and Fundamentals*. Elsevier, 2013.

[2] Y Mi and MH Aliabadi. Three-dimensional crack growth simulation using BEM. *Computers And Structures*, 52(5):871–878, 1994.

[3] RN Simpson, SPA Bordas, J Trevelyan, and T Rabczuk. A two-dimensional isogeometric boundary element method for elastostatic analysis. *Computer Methods in Applied Mechanics and Engineering*, 209-212:87–100, 2012.

[4] RN Simpson, SPA Bordas, H Lian, and J Trevelyan. An isogeometric boundary element method for elastostatic analysis: 2D implementation aspects. *Computers & Structures*, 118:2–12, March 2013.

[5] T Belytschko, YY Lu, and L Gu. Element-free Galerkin methods. *International Journal for Numerical Methods in Engineering*, 37(April 1993):229–256, 1994.

[6] T Belytschko, YY Lu, and L Gu. Crack propagation by element-free Galerkin methods. *Engineering Fracture Mechanics*, 51(2):295–315, 1995.

[7] M Fleming, Y A R Chu, B S Moran, and T Belytschko. Enriched element-free Galerkin methods for crack tip fields. *International Journal for Numerical Methods in Engineering*, 1504(January 1996):1483–1504, 1997.

[8] A Carpinteri, G Ferro, and G Ventura. An augmented Lagrangian element-free (ALEF) approach for crack discontinuities. *Computer Methods in Applied Mechanics and Engineering*, 191(8-10):941–957, December 2001.

[9] T Rabczuk, SPA Bordas, and G Zi. A three-dimensional meshfree method for continuous multiple-crack initiation, propagation and junction in statics and dynamics. *Computational Mechanics*, 40(3):473–495, March 2007.

[10] SPA Bordas, T Rabczuk, and G Zi. Three-dimensional crack initiation, propagation, branching and junction in non-linear materials by an extended meshfree method without asymptotic. *Engineering Fracture Mechanics*, 75:943–960, 2008.

[11] T Rabczuk, SPA Bordas, and G Zi. On three-dimensional modelling of crack growth using partition of unity methods. *Computers & Structures*, 88(23-24):1391–1411, December 2010.

[12] JM Melenk and I Babuska. The partition of unity finite element method: basic theory and applications. *Computer methods in applied mechanics and engineering*, 139(1-4):289–314, 1996.

[13] T Belytschko and T Black. Elastic crack growth in finite elements with minimal remeshing. *International Journal for Numerical Methods in Engineering*, 620(July 1998):601–620, 1999.

[14] N Moës, J Dolbow, and T Belytschko. A finite element method for crack growth without remeshing. *International Journal for Numerical Methods in Engineering*, 46(1):131–150, 1999.

[15] N Sukumar, N Moës, B Moran, and T Belytschko. Extended finite element method for three-dimensional crack modelling. *International Journal for Numerical Methods in Engineering*, 48(November 1999):1549–1570, 2000.

[16] N Moës, A Gravouil, and T Belytschko. Non-planar 3D crack growth by the extended finite element and level sets-Part I: Mechanical model. *International Journal for Numerical Methods in Engineering*, 53(11):2549–2568, April 2002.

[17] A Gravouil, N Moës, and T Belytschko. Non-planar 3D crack growth by the extended finite element and level sets-Part II: Level set update. *International Journal for Numerical Methods in Engineering*, 53(11):2569–2586, April 2002.

[18] SPA Bordas and B Moran. Enriched finite elements and level sets for damage tolerance assessment of complex structures. *Engineering Fracture Mechanics*, 73(9):1176–1201, June 2006.

[19] SPA Bordas, PV Nguyen, C Dunant, A Guidum, and H Nguyen-Dang. An extended finite element library. *International Journal for Numerical Methods in Engineering*, 71(January):703–732, 2007.

[20] E Wyart, D Coulon, M Duflot, T Pardoen, JF Remacle, and F Lani. A substructured FE-shell/XFE-3D method for crack analysis in thin-walled structures. *International Journal for Numerical Methods in Engineering*, 72(March):757–779, 2007.

[21] E Wyart, M Duflot, D Coulon, P Martiny, T Pardoen, JF Remacle, and F Lani. Substructuring FEXFE approaches applied to three-dimensional crack propagation. *Journal of Computational and Applied Mathematics*, 215(2):626–638, June 2008.

[22] E Wyart, D Coulon, T Pardoen, JF Remacle, and F Lani. Application of the substructured finite element/extended finite element method (S-FE/XFE) to

the analysis of cracks in aircraft thin walled structures. *Engineering Fracture Mechanics*, 76(1):44–58, January 2009.

[23] P Laborde, J Pommier, Y Renard, and M Salaün. High-order extended finite element method for cracked domains. *International Journal for Numerical Methods in Engineering*, 64(3):354–381, September 2005.

[24] E Béchet, H Minnebo, N Moës, and B Burgardt. Improved implementation and robustness study of the X-FEM for stress analysis around cracks. *International Journal for Numerical Methods in Engineering*, 64(8):1033–1056, October 2005.

[25] E Chahine and P Laborde. Crack tip enrichment in the XFEM using a cutoff function. *International journal for numerical methods in engineering*, 75(January):629–646, 2008.

[26] A Menk and SPA Bordas. A robust preconditioning technique for the extended finite element method. *International Journal for Numerical Methods in Engineering*, 85(October 2010):1609–1632, 2011.

[27] J Chessa, H Wang, and T Belytschko. On the construction of blending elements for local partition of unity enriched finite elements. *International Journal for Numerical Methods in Engineering*, 57(7):1015–1038, June 2003.

[28] TP Fries. A corrected XFEM approximation without problems in blending elements. *International Journal for Numerical Methods in Engineering*, 75(November 2007):503–532, 2008.

[29] R Gracie, H Wang, and T Belytschko. Blending in the extended finite element method by discontinuous Galerkin and assumed strain methods. *International*

Journal for Numerical Methods in Engineering, 74(November 2007):1645–1669, 2008.

[30] JE Tarancón, A Vercher, E Giner, and FJ Fuenmayor. Enhanced blending elements for XFEM applied to linear elastic fracture mechanics. *International Journal for Numerical Methods in Engineering*, 77(July 2008):126–148, 2009.

[31] G Ventura, R Gracie, and T Belytschko. Fast integration and weight function blending in the extended finite element method. *International journal for numerical methods in engineering*, 77(July 2008):1–29, 2009.

[32] S Loehnert, DS Mueller-Hoeppe, and P Wriggers. 3D corrected XFEM approach and extension to finite deformation theory. *International Journal for Numerical Methods in Engineering*, 86(October 2010):431–452, 2011.

[33] G Ventura. On the elimination of quadrature subcells for discontinuous functions in the eXtended Finite-Element Method. *International Journal for Numerical Methods in Engineering*, 66(5):761–795, April 2006.

[34] K Park, JP Pereira, CA Duarte, and GH Paulino. Integration of singular enrichment functions in the generalized/extended finite element method for three-dimensional problems. *International Journal for Numerical Methods in Engineering*, 78(December 2008):1220–1257, 2009.

[35] SE Mousavi and N Sukumar. Generalized Gaussian quadrature rules for discontinuities and crack singularities in the extended finite element method. *Computer Methods in Applied Mechanics and Engineering*, 199(49-52):3237–3249, December 2010.

[36] S Natarajan, DR Mahapatra, and SPA Bordas. Integrating strong and weak discontinuities without integration subcells and example applications in an XFEM/GFEM framework. *International Journal for Numerical Methods in Engineering*, 83(January):269–294, 2010.

[37] H Minnebo. Three-dimensional integration strategies of singular functions introduced by the XFEM in the LEFM. *International Journal for Numerical Methods in Engineering*, 92(July):1117–1138, 2012.

[38] N Chevaugeon, N Moës, and H Minnebo. Improved crack tip enrichment functions and integration for crack modeling using the extended finite element method. *Journal for Multiscale Computational Engineering*, 11:597–631, 2013.

[39] QZ Xiao and BL Karihaloo. Direct evaluation of accurate coefficients of the linear elastic crack tip asymptotic field. *Fatigue & Fracture of Engineering Materials & Structures*, 26(November 2002):719–729, 2003.

[40] XY Liu, QZ Xiao, and BL Karihaloo. XFEM for direct evaluation of mixed mode SIFs in homogeneous and bi-materials. *International Journal for Numerical Methods in Engineering*, 59(8):1103–1118, February 2004.

[41] A Zamani, R Gracie, and MR Eslami. Cohesive and non-cohesive fracture by higher-order enrichment of XFEM. *International Journal for ...*, 90(January):452–483, 2012.

[42] SPA Bordas and M Duflot. Derivative recovery and a posteriori error estimate for extended finite elements. *Computer Methods in Applied Mechanics and Engineering*, 196(35-36):3381–3399, July 2007.

[43] M Duflot and SPA Bordas. A posteriori error estimation for extended finite elements by an extended global recovery. *International Journal for Numerical Methods in Engineering*, 76(June):1123–1138, 2008.

[44] JJ Ródenas, OA González-Estrada, JE Tarancón, and FJ Fuenmayor. A recovery-type error estimator for the extended finite element method based on singular+ smooth stress field splitting. *International Journal for Numerical Methods in Engineering*, 76(March):545–571, 2008.

[45] JJ Ródenas, OA González-Estrada, P Díez, and FJ Fuenmayor. Accurate recovery-based upper error bounds for the extended finite element framework. *Computer Methods in Applied Mechanics and Engineering*, 199(37-40):2607–2621, August 2010.

[46] OA González-Estrada, JJ Ródenas, SPA Bordas, M Duflot, P Kerfriden, and E Giner. On the role of enrichment and statical admissibility of recovered fields in a posteriori error estimation for enriched finite element methods. *Engineering Computations*, 29(8):814–841, November 2012.

[47] E Chahine, P Laborde, and Y Renard. A non-conformal eXtended Finite Element approach: Integral matching Xfem. *Applied Numerical Mathematics*, 61(3):322–343, March 2011.

[48] M Duflot. A study of the representation of cracks with level sets. *International Journal for Numerical Methods in Engineering*, 70(November 2006):1261–1302, 2007.

[49] G Ventura, E Budyn, and T Belytschko. Vector level sets for description of

propagating cracks in finite elements. *International Journal for Numerical Methods in Engineering*, 58(10):1571–1592, November 2003.

[50] TP Fries and M Baydoun. Crack propagation with the extended finite element method and a hybrid explicitimplicit crack description. *International Journal for Numerical Methods in Engineering*, 89(November 2011):1527–1558, 2012.

[51] T Belytschko, N Moës, S Usui, and C Parimi. Arbitrary discontinuities in finite elements. *International Journal for Numerical Methods in Engineering*, 50(August 2000):993–1013, 2001.

[52] CR Langlois, A Gravouil, MC Baieto, and J Réthoré. Three-dimensional simulation of crack with curved front with direct estimation of stress intensity factors. *International Journal for Numerical Methods in Engineering*, 2014.

[53] J Fish. The s-version of the finite element method. *Computers & Structures*, 43(3):539–547, 1992.

[54] S Natarajan, SPA Bordas, and DR Mahapatra. Numerical integration over arbitrary polygonal domains based on SchwarzChristoffel conformal mapping. *International Journal for Numerical Methods in Engineering*, 80(July):103–134, 2009.

[55] MC Walters, GH Paulino, and RH Dodds. Interaction integral procedures for 3-D curved cracks including surface tractions. *Engineering Fracture Mechanics*, 72(11):1635–1663, July 2005.

[56] Y Renard and J Pommier. Gmm++ library. http://download.gna.org/getfem/html/homepage/gmm/index.html,

2004-2014.

[57] ML Kachanov, B Shafiro, and I Tsukrov. *Handbook of elasticity solutions*. 2003.

[58] VF González-Albuixech, E Giner, JE Tarancón, FJ Fuenmayor, and A Gravouil. Domain integral formulation for 3-D curved and non-planar cracks with the extended finite element method. *Computer Methods in Applied Mechanics and Engineering*, 264:129–144, September 2013.

[59] H Rajaram, S Socrate, and DM Parks. Application of domain integral methods using tetrahedral elements to the determination of stress intensity factors. *Engineering Fracture Mechanics*, 66(5):455–482, July 2000.